Updated tomographic analysis of the integrated Sachs-Wolfe effect and implications for dark energy

Benjamin Stölzner,[1,*] Alessandro Cuoco,[1,†] Julien Lesgourgues,[1,‡] and Maciej Bilicki[2,3,4,§]

[1]*Institute for Theoretical Particle Physics and Cosmology (TTK), RWTH Aachen University, Otto-Blumenthal-Strasse, 52057, Aachen, Germany*
[2]*Leiden Observatory, Leiden University, P.O. Box 9513, NL-2300 RA Leiden, The Netherlands*
[3]*National Centre for Nuclear Research, Astrophysics Division, P.O. Box 447, 90-950 Łódź, Poland*
[4]*Janusz Gil Institute of Astronomy, University of Zielona Góra, ul. Lubuska 2, 65-265 Zielona Góra, Poland*

We derive updated constraints on the integrated Sachs-Wolfe (ISW) effect through cross-correlation of the cosmic microwave background with galaxy surveys. We improve with respect to similar previous analyses in several ways. First, we use the most recent versions of extragalactic object catalogs, SDSS DR12 photometric redshift (photo-z) and 2MASS Photo-z data sets, as well as those employed earlier for ISW, SDSS QSO photo-z and NVSS samples. Second, we use for the first time the WISE × SuperCOSMOS catalog, which allows us to perform an all-sky analysis of the ISW up to $z \sim 0.4$. Third, thanks to the use of photo-zs, we separate each data set into different redshift bins, deriving the cross-correlation in each bin. This last step leads to a significant improvement in sensitivity. We remove cross-correlation between catalogs using masks which mutually exclude common regions of the sky. We use two methods to quantify the significance of the ISW effect. In the first one, we fix the cosmological model, derive linear galaxy biases of the catalogs, and then evaluate the significance of the ISW using a single parameter. In the second approach we perform a global fit of the ISW and of the galaxy biases varying the cosmological model. We find significances of the ISW in the range 4.7–5.0σ thus reaching, for the first time in such an analysis, the threshold of 5σ. Without the redshift tomography we find a significance of $\sim$4.0σ, which shows the importance of the binning method. Finally we use the ISW data to infer constraints on the dark energy redshift evolution and equation of state. We find that the redshift range covered by the catalogs is still not optimal to derive strong constraints, although this goal will be likely reached using future datasets such as from Euclid, LSST, and SKA.

I. INTRODUCTION

We have, at present, strong evidence for dark energy (DE) from the large amount of available cosmological data [e.g., [1]]. Nonetheless, this evidence is mostly based on precise constraints from the cosmic microwave background (CMB) epoch extrapolated to the present time. Local, or present-day, constraints on DE are, instead, mostly given by SuperNovae (SN) data, which are not yet precise enough for accurately constraining the properties and time evolution of DE [e.g., [2]].

Thus, it is important to look for alternative local DE probes. In this respect such a DE-sensitive measurement is given by the late-time integrated Sachs-Wolfe effect (ISW) on the CMB [3]. This effect is imprinted in the angular pattern of the CMB in the presence of a time-varying

cosmological gravitational potential, which appears in the case of a nonflat universe [4,5], as well as for a flat one in the presence of DE, but also for various modified gravity theories [e.g., [6,7]]. Thus, for standard general relativity (GR) and flat cosmology a nonzero ISW implies the presence of DE. The effect is very small and cannot be well measured using the CMB alone since it peaks at large angular scales (small multipoles, $\ell \lesssim 40$) which are cosmic-variance limited. On the other hand, it was realized that this effect can be more efficiently isolated by cross-correlating the CMB with tracers of the large-scale structure (LSS) of the Universe at low ($z \lesssim 1$) redshift [8,9], with most of the signal lying in the range $z \in [0.3, 1.5]$ for a standard ΛCDM cosmological model [10].

In the past, many ISW analyses were performed using a large variety of tracers at different redshifts [11–28]. In a few cases, global analyses were performed combining different LSS tracers, giving the most stringent constraints and evidence for the ISW effect at the level of $\sim$4σ [29–31]. Related methodology, which has been explored more

*stoelzner@physik.rwth-aachen.de
†cuoco@physik.rwth-aachen.de
‡lesgourg@physik.rwth-aachen.de
§bilicki@strw.leidenuniv.nl

recently, consists in stacking CMB patches overlapping with locations of large-scale structures, such as superclusters or voids [32–38]. A further idea, which was sometimes exploited, is to use the redshift information of a given catalog to divide it into different redshift bins, compute the cross-correlation in each bin, and then combine the information. This tomographic approach was pursued, for example, in the study of 2MASS [39] or SDSS galaxies [40,41]. Typically, the use of tomography does not provide strong improvement over the no-binning case, either because the catalog does not contain a large enough number of objects and splitting them increases the shot-noise or because the redshift range is not well suited for ISW studies.

Nonetheless, in the recent years, several catalogs with redshift information and with a very large number of objects have become available thanks to the use of photometric redshifts (photo-zs) instead of spectroscopic ones. Although photo-zs are not as accurate as their spectroscopic counterparts, the former are sufficient for performing a tomographic analysis of the ISW with coarse z bins. Hence we can exploit these large catalogs, which have the advantage of giving a low shot noise even when divided into sub-samples. In this work, we combine for the first time the two above approaches: we use several data sets covering different redshifts ranges, and we bin them into redshift sub-samples to perform a global tomography. We show that in this way we are able to improve the significance of the ISW effect from $\sim 4\sigma$ without redshift binning to $\sim 5\sigma$ exploiting the full tomography information. When combining the various catalogs, we take special care to minimize their overlap both in terms of common sources and the same LSS traced, in order not to use the same information many times. This is done by appropriate data cleaning and masking. We then use these improved measurement of the ISW effect to study deviations of DE from the simplest assumption of a cosmological constant.

Finally, the correlation data derived in this work and the associated likelihood will soon be made publicly available, in the next release of the MONTEPYTHON[1] package [42].

II. THEORY

The expression for the cross-correlation angular power spectrum (CAPS) between two fields I and J is given by:

$$C_l^{I,J} = \frac{2}{\pi} \int k^2 P(k) [G_\ell^I(k)][G_\ell^J(k)] dk, \qquad (1)$$

where $P(k)$ is the present-day power spectrum of matter fluctuations. In the above expression we have assumed an underlying cosmological model, like ΛCDM, in which the evolution of density fluctuations is separable in wavenumber k and redshift z on linear scales. A different expression applies, for example, in the presence of massive

neutrinos [43], where the k and z evolution is not separable. Moreover, in the following, we assume standard GR and a flat ΛCDM model. For studies of the ISW effect for nonzero curvature or modified gravity see [4–7].

For the case $I = c$ of the fluctuation field of a catalog of discrete objects, one has

$$G_\ell^c(k) = \int \frac{dN(z)}{dz} b_c(z) D(z) j_\ell[k\chi(z)] dz, \qquad (2)$$

where $dN(z)/dz$ and $b_c(z)$ represent the redshift distribution and the galaxy bias factor of the sources, respectively, $j_\ell[k\chi(z)]$ are spherical Bessel functions, $D(z) = (P(k,z)/P(k))^{1/2}$ is the linear growth factor of density fluctuations and $\chi(z)$ is the comoving distance to redshift z.

For the case of cross-correlation with the temperature fluctuation field obtained from the CMB maps ($J = T$), the ISW effect in real space is given by [e.g., [44]]

$$\Theta(\hat{n}) = -2 \int \frac{d\Phi(\hat{n}\chi,\chi)}{d\chi} d\chi, \qquad (3)$$

where Φ represents the gravitational potential. In the expression, we neglect a factor of $\exp(-\tau)$, which introduces an error of the order of 10%, smaller than the typical accuracy achieved in the determination of the ISW itself. Furthermore, using the Poisson and Friedmann equations,[2] and considering scales sufficiently within the horizon

$$\Phi(k,z) = -\frac{3}{2c^2} \frac{\Omega_m}{a(z)} \frac{H_0^2}{k^2} \delta(k,z) \qquad (4)$$

where c is the speed of light, $a(z)$ is the cosmological scale factor, H_0 is the Hubble parameter today, $\Omega_m = \Omega_b + \Omega_c$ is the fractional density of matter today, and $\delta(k,z)$ is the matter fluctuation field in Fourier space, we can write

$$G_\ell^T(k) = \frac{3\Omega_m}{c^2} \frac{H_0^2}{k^2} \int \frac{d}{dz}\left(\frac{D(z)}{a(z)}\right) j_\ell[k\chi(z)] dz. \qquad (5)$$

Finally, the equations above can be combined through Eq. (1) to give the CAPS expected for the ISW effect resulting from the correlation between a catalog of extragalactic objects, tracing the underlying mass distribution, and the CMB. Using the Limber approximation [45] the correlation becomes [31]

$$C_\ell^{cT} = \frac{3\Omega_m H_0^2}{c^3(l+\frac{1}{2})^2} \int dz\, b_c(z) \frac{dN}{dz} H(z) D(z) \frac{d}{dz}\left(\frac{D(z)}{a(z)}\right)$$
$$\times P\left(k = \frac{l+\frac{1}{2}}{\chi(z)}\right). \qquad (6)$$

---

[1]See http://baudren.github.io/montepython.html.

[2]Eqs. (3)–(4) are valid assuming GR. For modified gravity different appropriate expressions would apply (see, e.g., [6,7]).

The Limber approximation is very accurate at $\ell > 10$ and accurate at the level of 10% at $\ell < 10$ [45], which is sufficient for the present analysis.

In our study, we use the public code CLASS[3] [46] to compute the linear power spectrum of density fluctuations. As an option, this code can compute internally the spectra C_ℓ^{cT} and C_ℓ^{cc}, for arbitrary redshift distribution functions, using either the Limber approximation or a full integral in (k, z) space. We prefer, nonetheless, to use the Limber approximation since CAPS calculations are significantly faster. Also, to get better performances and more flexibility, we choose to perform these calculations directly inside our python likelihood, reading only $P(k, z)$ from the CLASS output. We checked on a few examples that our spectra do agree with those computed internally by CLASS.

III. CMB MAPS

We use CMB maps from the Planck 2015 data release[4] [1] which have been produced using four different methods of foreground subtraction: Commander, NILC, SEVEM, and SMICA. Each method provides a confidence mask which defines the region of the sky in which the CMB maps can be used. We construct a combined mask as the union of these four confidence masks. This mask is applied on the CMB maps before calculating the cross-correlation. We will use the SEVEM map as default for the analysis. Nonetheless, we have also tested the other maps to check the robustness of the results. The test is described in more detail in Sec. VIII.

As the ISW effect is achromatic, for further cross-checks we also use CMB maps at different frequencies. In particular we use maps at 100 GHz, 143 GHz, and 217 GHz. The results using these maps are also described in Sec. VIII.

IV. ADDITIONAL COSMOLOGICAL DATA SETS

In the following we will perform parameter fits using the ISW data obtained with the cross-correlation. Beside this, in some setups, we will also use other cosmological data sets in conjunction. In particular, we will employ the Planck 2015 public likelihoods[5] [1] and the corresponding MONTEPYTHON interfaces Planck_highl_lite (for high-ℓ temperature), Planck_lowl (for low-ℓ temperature and polarization), and Planck_lensing (CMB lensing reconstruction). The accuracy of the Planck_highl_lite likelihood (which performs an internal marginalization over all the nuisance parameters except one) with respect to the full Planck likelihood (where the nuisance parameters are not marginalized)
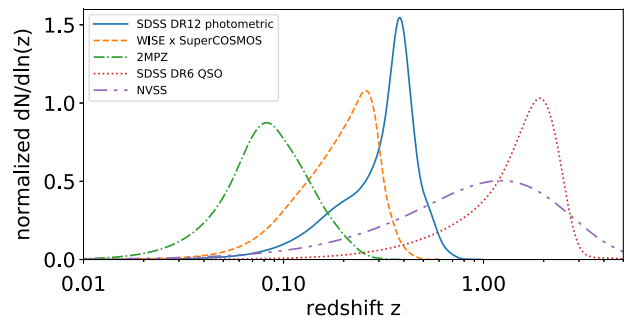

FIG. 1. Photometric redshift distributions for the five catalogs used for the cross-correlation. The dN/dz curves are normalized to a unit integral. For the NVSS case the analytical approximation described in the text is used, since no redshifts information is available for the single catalog objects.

has been tested in [47,48] where the authors find that the difference in the inferred cosmological parameters is at the level of 0.1σ. Finally we will use BAO data from 6dF [49], SDSS DR7 [50] and BOSS DR10&11 [51], which are implemented as bao_boss and bao_boss_aniso in MONTEPYTHON.

V. CATALOGS OF DISCRETE SOURCES

For the cross-correlation with the CMB, as tracers of matter distribution we use five catalogs of extragalactic sources. As the ISW is a wide-angle effect, they were chosen to cover as large angular scales as possible, and two of them are all-sky. Furthermore, our study does not require exact, i.e. spectroscopic, redshift information, thus photometric samples are sufficient. Except for one case, the data sets employed here include individual photo-zs for each source, which allows us to perform a tomographic approach by splitting the data sets into redshift bins.

The catalogs we use span a wide redshift range; see Fig. 1 for their individual redshift distributions. Table I quantifies their properties (sky coverage, number of sources, mean projected density) as effectively used for the analysis, i.e., after applying both the catalog and CMB masks.

For a plot of the sky maps and masks of the catalogs described below, and for their detailed description, see [52]. Below we provide a short summary of the properties of the data sets.

A. 2MPZ

As a tracer of the most local LSS in this study we use the 2MASS Photometric Redshift catalog[6] [2MPZ, [53]]. This data set was built by merging three all-sky photometric data sets covering optical, near-infrared (IR), and mid-IR passbands: SuperCOSMOS scans of UKST/POSS-II photographic plates [54], 2MASS Extended Source Catalog [55],

TABLE I. Statistics of the catalogs used in the analysis. The numbers refer to the area of the sky effectively employed in the analysis, i.e., applying both the catalog and CMB masks.

Source catalog	Sky coverage	Number of sources	Mean surface density [deg^{-2}]
NVSS	62.3%	431,724	67.2
2MPZ	64.2%	661,060	24.9
WISE × SCOS	64.5%	17,695,635	665
SDSS DR12	18.7%	23,907,634	3095
SDSS DR6 QSO	15.6%	461,093	71.8

and Wide-field Infrared Survey Explorer [WISE, [56]]. Photo-zs were subsequently estimated for all the included sources, by calibrating on overlapping spectroscopic data sets.

2MPZ includes ~935,000 galaxies over almost the full sky. Part of this area is however undersampled due to the Galactic foreground and instrumental artifacts, we thus applied a mask described in [57]. When combined with the CMB mask, this leaves over 660,000 2MPZ galaxies on ~64% of the sky (Table I).

2MPZ provides the best-constrained photo-zs among the catalogs used in this paper. They are practically unbiased ($\langle \delta z \rangle \sim 0$) and their random errors have RMS scatter $\sigma_{\delta z} \simeq 0.015$, to a good accuracy independent of redshift. We show the 2MPZ redshift distribution in Fig. 1 with the dot-dashed green line; the peak is at $z \sim 0.06$ while the mean $\langle z \rangle \sim 0.08$. The overall surface density of 2MPZ is ~25 sources per square degree.

For the tomographic analysis we split the catalog in three redshift bins: $z \in [0.00, 0.105]$, $[0.105, 0.195]$ and $[0.195, 0.30]$. The first two include the bulk of the distribution, approximately divided into two comparable sub-samples, while the third bin explores the tail of the dN/dz where most of the ISW signal is expected.

A precursor of 2MPZ, based on 2MASS and SuperCOSMOS only, was used in a tomographic ISW analysis by [39], while an early application of 2MPZ itself to ISW tomography is presented in [58]. In both cases no significant ISW signal was found, consistent with expectations. Another ISW-related application of 2MPZ is presented in [13], where it was applied to reconstruct ISW anisotropies caused by the LSS.

B. WISE × SuperCOSMOS

The WISE × SuperCOSMOS photo-z catalog[7] [WI × SC, [59]] is an all-sky extension of 2MPZ obtained by cross-matching WISE and SuperCOSMOS samples. WI × SC reaches roughly 3 times deeper than 2MPZ and has almost 30 times larger surface density. However, it suffers from more severe foreground contamination, and its

[7]Available from http://ssa.roe.ac.uk/WISExSCOS.html.

useful area is ~70% of the sky after applying its default mask. This is further reduced to ~65% once the Planck mask is also used; the resulting WI × SC sample includes about 17.5 million galaxies.

WI × SC photo-zs have overall mean error $\langle \delta z \rangle \sim 0$ and distance-dependent scatter of $\sigma_{\delta z} \simeq 0.033(1 + z)$. The redshift distribution is shown in Fig. 1 with the dashed orange curve. The peak is at $z \sim 0.2$, and the majority of the sources are within $z < 0.5$. In the tomographic approach, the WI × SC sample is divided into four redshift bins: $z \in [0.00, 0.09]$, $[0.09, 0.21]$, $[0.21, 0.30]$, and $[0.30, 0.60]$, with approximately equal number of galaxies in each bin.

As far as we are aware, our study employs the WI × SC data set for an ISW analysis for the first time. Various studies based using WISE have been performed in the past [23,25,60,61]. However, the samples used there differed significantly from WI × SC, and none included individual redshift estimates which would allow for redshift binning.

C. SDSS DR12 photometric

Currently there are no all-sky photo-z catalogs available reaching beyond WI × SC. Therefore, in order to look for the ISW signal at $z > 0.5$, we used data sets of smaller sky coverage. The first of them, with the largest number density of all employed in this paper, is based on the Sloan Digital Sky Survey Data Release 12 (SDSS-DR12) photo-z sample compiled by [62]; to our knowledge, our study is its first application to an ISW analysis, although earlier versions (DR 6 and DR 8) were used in [29,30] (but without z binning).

The parent SDSS-DR12 photo-z data set includes over 200 million galaxies. Here, however, we use a subsample described in detail in [52], which was obtained via appropriate cleaning as recommended by [62], together with our own subsequent purification of problematic sky areas. In particular, as the SDSS galaxies are distributed in two disconnected regions in the Galactic south and north, with most of the area in the northern part, and uneven sampling in the south, we have excluded the latter region from the analysis. After additionally employing the Planck CMB mask, we were left with about 24 million SDSS DR12 sources with mean $\langle z \rangle = 0.34$ and mostly within $z < 0.6$. The resulting sky coverage is ~19% and the mean surface density is ~3100 deg^{-2}. The redshift distribution is shown in Fig. 1 with the solid blue line.

Thanks to the very large projected density of objects, we were able to split the SDSS-DR12 sample into several redshift bins, keeping low shot-noise in each shell. For the tomographic analysis we divided the data set into six bins: $z \in [0.0, 0.1]$, $[0.1, 0.3]$, $[0.3, 0.4]$, $[0.4, 0.5]$, $[0.5, 0.7]$ and $[0.7, 1.0]$. The range $z \in [0.1, 0.3]$ is not subdivided further since this redshift range is best covered by WI × SC, where we already have sub-bins. The photo-z accuracy of SDSS-DR12 depends on the "photo-z class" defined by [62], and each class has an associated error estimate. Our specific

preselection detailed in [52] leads to an effective photo-z scatter of $\sigma_{\delta z} = 0.022(1 + z)$ based on the overall error estimates from [62].

D. SDSS DR6 QSO

As a tracer of high-z LSS, we use a catalog of photometric quasars (QSOs) compiled by [63] from the SDSS DR6 data set (DR6-QSO in the following), used previously in ISW studies by e.g. [22,29,30]. We apply the same preselections as in [22], and the resulting sample includes 6×10^5 QSOs on ~25% of the sky. We exclude from the analysis three narrow stripes present in the south Galactic sky and use only the northern region.

The DR6-QSO sources are provided with photo-zs spanning formally $0 < z < 5.75$ but with a relatively peaked dN/dz and mean $\langle z \rangle \simeq 1.5$ (dotted red line in Fig. 1). For tomographic analysis, this QSO data set will be split into three bins of $z \in [0.5, 1.0]$, $[1.0, 2.0]$, and $[2.0, 3.0]$, selected in a way to have similar number of objects in each bin. We excluded the QSOs in the range $z \in [0.0, 0.5]$ in order to minimize the overlap with the other catalogs in this redshift range. Nonetheless, there are very few DR6-QSO catalog objects at these redshifts, thus this choice has only a very minor impact on the results. The typical photo-z accuracy of this data set is $\sigma_{\delta z} \sim 0.24$ as reported by [63], and we will use this number for the extended modeling of underlying dN/dz s per redshift bin in Sec. VIII.

E. NVSS

The NRAO VLA Sky Survey [NVSS, [64]] is a catalog of radio sources, most of which are extragalactic. This sample has already been used for multiple ISW studies [e.g. [9,20,26–28]]. The data set covers the whole sky available for the VLA instrument; after appropriate cleanup of likely Galactic entries and artifacts, the NVSS sample includes $\sim 5.7 \times 10^5$ objects flux-limited to > 10 mJy, located at declinations $\delta \gtrsim -40°$ and Galactic latitudes $|b| > 5°$. This is the only of the data sets considered in this work which does not provide even crude redshift information for the individual sources. We thus use it without tomographic binning and, where relevant, assume its dN/dz to follow the model of [65] (purple short-long-dashed line in Fig. 1). This sample spans the broadest redshift range of all the considered catalogs, namely $0 < z < 5$.

F. Masks

In the correlation of the CMB with each catalog we use the CMB mask, described in Sec. III, combined with the specific mask of the given catalog. Beside this, we define specific masks which we use when combining the signal from the different catalogs in order to circumvent including the same information twice, and to avoid the need to take into account the cross-correlations between various tracers of the same LSS. We proceeded in the following way.

(i) SDSS catalogs (i.e. SDSS DR6 QSOs and SDSS DR12 galaxies) are used without additional masks. When combining the information with other catalogs we, however, exclude the first SDSS DR12 bin, since the region $z \in [0.0, 0.1]$ is best covered by 2MPZ.

(ii) To avoid correlations with the SDSS catalogs, when using all the remaining ones (i.e. NVSS, 2MPZ, WI × SC) we apply a mask which is a complementary of the joint mask of SDSS DR12 galaxies and SDSS DR6 QSOs (in short, SDSS mask in the following).

(iii) For 2MPZ and WI × SC, it is not possible to define mutually exclusive masks since both these data sets cover practically the same part of the sky. Nonetheless, we use them together, since WI × SC was built excluding most of the objects already contained in 2MPZ [59]. The two catalogs, thus, have practically no common sources. In this way the correlation among the two data sets is significantly suppressed, although not totally, since both trace the same underlying LSS in the overlapping redshift ranges. We will, however, not consider the first bin, $z \in [0.0, 0.1]$, of WI × SC in the combined analysis since in this redshift range 2MPZ has better redshift determination and basically no stellar contamination. Nonetheless, as we will show in Sec. VII, the evidence for ISW in the range $z \in [0.0, 0.2]$, where 2MPZ and WI × SC have most of the overlap, is very small, so, in practice, this has only a marginal effect on the final ISW significance.

(iv) Similarly, also for NVSS, 2MPZ and WI × SC, it is not possible to define a mutually exclusive mask due to the large common area of the sky. In this case, we note that 2MPZ and WI × SC cover only the low redshift tail of NVSS. Thus, the overlap and correlation among them is minimal.

We will, thus, use the above setup when reporting combined significances of the ISW from the different catalogs. For simplicity, we will use the same setup also to derive autocorrelations of the single catalogs. In this case the significances could be increased slightly for NVSS, 2MPZ, and WI × SC if their proper masks were used, but we checked that the improvement is only marginal.

VI. CROSS-CORRELATION ANALYSIS

In the previous section we have presented the catalogs of extragalactic objects that we use in the analysis. Their input format is that of a 2D pixelized map of object counts $n(\hat{\Omega}_i)$, where $\hat{\Omega}_i$ specifies the angular coordinate of the i-th pixel. For the cross-correlation analysis we consider maps of normalized counts $n(\hat{\Omega}_i)/\bar{n}$, where $\bar{n}$ is the mean object density in the unmasked area, and CMB temperature maps, also pixelized with a matching angular resolution.

In our analysis we compute both the angular 2-point cross-correlation function, CCF, $w^{(cT)}(\theta)$, and its harmonic transform, the angular power spectrum $\bar{C}_\ell^{(cT)}$, CAPS. However, we restrict the quantitative analysis to the CAPS only. The reason for this choice is that the CAPS has the advantage that different multipoles are almost uncorrelated, especially after binning. Their covariance matrix is therefore close to diagonal, which simplifies the comparison between models and data. Similarly, we compute also the autocorrelation power spectrum of the catalogs (APS) and the related autocorrelation function (ACF).

We use the *PolSpice*[8] statistical toolkit [66–69] to estimate the correlation functions and power spectra. *PolSpice* automatically corrects for the effect of the mask. In this respect, we point out that the effective geometry of the mask used for the correlation analysis is obtained by combining that of the CMB maps with those of each catalog of astrophysical objects. The accuracy of the *PolSpice* estimator has been assessed in [70] by comparing the measured CCF with the one computed using the popular Landy-Szalay method [71]. The two were found to be in very good agreement. *PolSpice* also provides the covariance matrix for the angular power spectrum, $\bar{V}_{\ell\ell'}$ [72].

For the case of source catalog APS a further step is required. Contrary to the CAPS, the APS contains shot noise due to the discrete nature of the objects in the map. The shot noise is constant in multipole and can be expressed as $C_N = 4\pi f_{sky}/N_{gal}$, where f_{sky} is the fraction of sky covered by the catalog in the unmasked area and N_{gal} is the number of catalog objects, again in the unmasked area. The above shot-noise has been subtracted from our final estimated APS.

The Planck Point Spread Function and the map pixelization affect in principle the estimate of the CAPS. However, the CAPS contains information on the ISW only up to $\ell \sim 100$ where these effects are negligible. We will thus not consider them further.

Finally, to reduce the correlation in nearby multipoles induced by the angular mask, we use an ℓ-binned version of the measured CAPS. The number of bins and the maximum and minimum ℓ used in the analysis will be varied to assess the robustness of the results. We indicate the binned CAPS with the same symbol as the unbinned one, $C_\ell^{(cT)}$. It should be clear from the context which one is used. The $C_\ell^{(cT)}$ in each bin is given by the simple unweighted average of the $C_\ell^{(cT)}$ within the bin. For the binned $C_\ell^{(cT)}$ we build the corresponding covariance matrix as a block average of the unbinned covariance matrix $V_{\ell\ell'}$, i.e., $\sum_{\ell\ell'} V_{\ell\ell'}/\Delta\ell/\Delta\ell'$, where $\Delta\ell$, $\Delta\ell'$ are the widths of the two multipole bins, and ℓ, ℓ' run over the multipoles of the first and the second bin. The binning procedure is very

efficient in removing correlation among nearby multipoles, resulting in a block covariance matrix that is, to a good approximation, diagonal. We will use nonetheless the full block covariance matrix in the following, although we have checked that using the diagonal only gives minor differences. When showing CAPS plots, however, we use the diagonal terms to plot the errors on the C_ℓ, $(\Delta C_\ell)^2 = \sum_{\ell\ell'} V_{\ell\ell'}/\Delta\ell^2$, where the sum runs over the multipoles of the bin contributing to C_ℓ.

VII. DERIVATION OF THE ISW SIGNIFICANCE

In this section, we illustrate the two methods we use to quantify the significance of the ISW. We will assume for the first method a flat ΛCDM model with cosmological parameters $\Omega_b h^2 = 0.022161$, $\Omega_c h^2 = 0.11889$, $\tau = 0.0952$, $h = 0.6777$, $\ln 10^{10} A_s = 3.0973$ at $k_0 = 0.05$ Mpc^{-1}, and $n_s = 0.9611$, in accordance with the most recent Planck results [1].

A. Method 1

This is the usual method employed in previous publications to study the significance of the ISW. In this case we fix the cosmological model to the best-fit one measured by Planck, and we derive with CLASS the matter power spectrum $P(k, z)$, which is used to calculate the expected autocorrelation C_ℓ for each catalog for the appropriate redshift bin. The measured autocorrelation is then used to fit the linear bias, as a proportionality constant in the predicted C_ℓ. An example of this fit is shown in the left panel of Fig. 2. A simple χ^2 over the bins of the autocorrelation is used for the fit:

$$\chi_{AC}^2 \equiv \chi^2(b^2) = \sum_{\ell \text{ bins}} \frac{(\hat{C}_\ell^c(b^2) - C_\ell^c)^2}{(\Delta C_\ell^c)^2}, \qquad (7)$$

where $\hat{C}_\ell^c$ and C_ℓ^c represent the model and the measured CAPS, and the sum is over all ℓ bins.

As mentioned in Sec. VI we tested that the use of the full covariance matrix with respect to the diagonal expression for the χ^2 above does not give appreciable differences. Table II summarizes the various measured biases, and the default binning used for the autocorrelations. We tested the robustness of the fitted biases changing the number of bins from four to six and the maximum ℓ from 40–80, and we found stable results, with variations of the order of 10%. A maximum ℓ of 40–80 is chosen since above this range typically nonlinear effects become significant. As the default case, we use four bins in the range 10–60.

As a further test, we checked the impact of using nonlinear corrections to the matter power spectrum to model the autocorrelation of the catalogs. The nonlinear corrections were implemented through the version of Halofit [73] implemented in CLASS v2.6.1. The last two columns of Table II show the bias and the best-fit χ^2 obtained using the

---

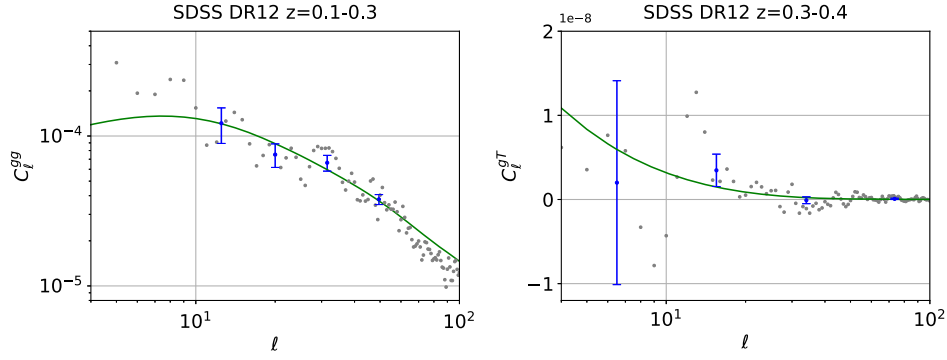[8]See http://www2.iap.fr/users/hivon/software/PolSpice/.

FIG. 2. Left: Example of measured source catalog autocorrelation and best-fit model with free galaxy bias, referring to the case of SDSS-DR12 in the labeled z bin. Right: example of measured cross-correlation between sources and CMB temperature and best-fit model, referring to the case of SDSS-DR12 in the labeled z bin. Dots refer to the measured single multipoles, while data points with error bars refer to binned measurements.

nonlinear model. It can be seen that the biases obtained with and without nonlinear corrections are fully compatible. The only exception is the first redshift bin of 2MPZ where the best-fit bias changes at the 2σ level. More importantly, the fit shows a visible improvement from $\chi^2 \sim 4.4$ to $\chi^2 \sim 1.3$. This is expected, since at these low redshifts even the small ℓs correspond mostly to small, nonlinear, physical scales. As we show below, however,

2MPZ presents little or no imprint of the ISW effect, so we conclude that the use of the linear $P(k,z)$ has a negligible impact on the study of the ISW effect in this analysis.

As an additional comment about the galaxy biases reported in Table II, we note that the $\sim 10\%$ variation quoted above is typically larger than the statistical errors given in that Table, the latter being sometimes only a few

TABLE II. Linear biases for the different redshift bins of the various catalogs fitted for a fixed cosmological model. The reported errors on the bias are derived from the fit of Eq. (7); goodness of fit is quantified in the relevant χ^2 columns. The χ^2 refers to the case of a fit with 4 bins in the multipole range 10-60.

catalog	z	b	χ^2_{min}	$b_{Halofit}$	χ^2_{min}	$b_{Halofit+\sigma_{\delta z}}$	χ^2_{min}
SDSS	0–0.1	0.70 ± 0.02	3.59	0.69 ± 0.02	3.76	0.71 ± 0.02	4.11
	0.1–0.3	1.03 ± 0.03	1.71	1.03 ± 0.03	1.68	1.02 ± 0.03	1.63
	0.3–0.4	0.88 ± 0.03	0.64	0.88 ± 0.03	0.63	0.87 ± 0.03	0.61
	0.4–0.5	0.79 ± 0.02	4.84	0.80 ± 0.02	4.65	0.84 ± 0.03	4.99
	0.5–0.7	1.14 ± 0.04	6.16	1.13 ± 0.04	5.86	1.23 ± 0.04	6.35
	0.7–1	1.02 ± 0.11	15.04	1.03 ± 0.11	14.99	1.23 ± 0.13	15.16
WIxSC	0–0.09	0.62 ± 0.03	0.46	0.60 ± 0.03	0.38	0.57 ± 0.03	0.28
	0.09–0.21	0.89 ± 0.03	2.38	0.87 ± 0.03	2.67	0.88 ± 0.03	2.62
	0.21–0.3	0.80 ± 0.02	10.07	0.81 ± 0.02	10.14	0.80 ± 0.02	10.09
	0.3–0.6	0.96 ± 0.03	5.62	1.03 ± 0.04	5.88	1.24 ± 0.04	5.55
QSO	0–1	1.55 ± 0.16	5.9	1.56 ± 0.16	5.93	1.45 ± 0.15	4.97
	0.5–1	1.54 ± 0.26	3.09	1.55 ± 0.26	3.07	1.52 ± 0.26	3.07
	1–2	2.64 ± 0.27	3.61	2.66 ± 0.27	3.59	2.61 ± 0.27	3.6
	2–3	3.19 ± 0.50	7.08	3.21 ± 0.51	7.05	3.51 ± 0.55	7.08
2MPZ	0–0.105	1.09 ± 0.03	4.41	1.03 ± 0.03	1.30	1.03 ± 0.03	1.26
	0.105–0.195	1.12 ± 0.04	2.00	1.12 ± 0.04	2.07	1.19 ± 0.04	2.17
	0.195–0.3	1.84 ± 0.09	6.54	1.86 ± 0.09	6.67	2.03 ± 0.09	6.34
NVSS	0–6	2.18 ± 0.08	3.02	2.04 ± 0.08	0.64	$\cdots$	$\cdots$

catalog	z	b	χ^2_{min}	$b_{Halofit}$	χ^2_{min}		
SDSS	0–1	1.34 ± 0.04	1.25	1.35 ± 0.04	1.27	1.39 ± 0.04	1.59
WIxSC	0-0.6	1.08 ± 0.03	3.15	1.07 ± 0.03	3.74	1.12 ± 0.03	3.94
QSO	0–3	2.67 ± 0.23	2.77	2.68 ± 0.23	2.76	2.66 ± 0.23	2.4
2MPZ	0–0.3	1.23 ± 0.04	5.19	1.17 ± 0.04	2.04	1.20 ± 0.04	1.98

%; this means that the bias errors are systematics- rather than statistics-limited. Also, in some cases, for example most notably in the $z \in [0.7, 1.0]$ bin of SDSS DR12 galaxies, the minimum χ^2 is quite large, indicating a poor quality of the fit. This is also visible in some of the AC plots provided in Appendix. This is likely related to nonuniformities of the catalogs, which are more severe in the tails of the redshift distribution, which in particular leads to excessively large measured low-ℓ AC power in some cases. Therefore, in such instances, the small statistical errors on b should be taken with care. In general, we stress that the precise determination of the bias error is not crucial in this analysis, which is, instead, focused on the determination of the significance of the ISW effect. To this aim, the error, and even the value of the bias, have only a limited impact. See further discussion below.

In the second step, all the galaxy biases are fixed to best-fit values previously derived, and only the measured cross-correlations are used. At this point only a single parameter A_{ISW} is fitted using as data either a single measured cross-correlation or a combination of them, with the χ^2 statistics:

$$\chi^2_{CC} \equiv \chi^2(A_{\mathrm{ISW}}) = \sum_{z\text{-bins}} \sum_{\mathrm{cat}} \sum_{\ell\,\mathrm{bins}} \frac{(A_{\mathrm{ISW}} \hat{C}^{\mathrm{Tc}}_\ell - C^{\mathrm{Tc}}_\ell)^2}{(\Delta C^{\mathrm{Tc}}_\ell)^2}, \quad (8)$$

where $\hat{C}^{\mathrm{Tc}}_\ell$ and C^{Tc}_ℓ represent the model (for the standard ΛCDM cosmological model considered) and the measured catalog—CMB temperature cross-correlation for a given redshift bin, respectively, the sum is over all the ℓ bins, and over different catalogs and different redshift bins. The linear parameter A_{ISW} quantifies the agreement with the above standard model expectation. In the denominator, we use the error provided by *Polspice* discussed in the previous section. In principle, however, one should use an error where the model is taken into account. For the case of binned data, however, this is a small effect (see for example discussion in [74]).

An example of measured cross-correlation and fit to the model is shown in the right panel of Fig. 2. Table III summarizes the results of the fit for each single z-bin of each catalog, for each catalog combining the different z-bins, and for different combinations of the catalogs, where, again, for each catalog z-binning has been used. For the default case we use four multipole bins between ℓ of 4 and 100, but, again, we have verified that the results are stable when changing the number of bins from 4 to 6 and the maximum ℓ from 60 to 100, which is expected, since the ISW effect is rapidly decreasing as a function of ℓ, and not much signal is expected beyond $\ell \sim 60$.

To quantify the significance of the measurement we use as test-statistic the quantity

$$\mathrm{TS} = \chi^2(0) - \chi^2_{\mathrm{min}}, \quad (9)$$

where χ^2_{min} is the minimum χ^2, and $\chi^2(0)$ is the χ^2 of the null hypothesis of no ISW effect, i.e. of the case $A_{\mathrm{ISW}} = 0$. TS is expected to behave asymptotically as a χ^2 distribution with a number of degrees of freedom equal to the number of fitted parameters, allowing us to derive the significance level of a measurement based on the measured TS. In this case, since there is only one fitted parameter, the significance in sigma is just given by $\sqrt{\mathrm{TS}}$. From Table III one can see that the maximum significance achieved with Method 1 when using all the catalogs in combination is $\sqrt{22.16} = 4.7\sigma$. From the different results it can also be seen that the main contribution is given by NVSS and SDSS DR12 galaxies. We remind that the cross-correlation with NVSS is calculated masking the area of the sky used to calculate the correlation with SDSS. The two are, thus, completely independent. A smaller, and comparable, contribution, is given by WI × SC and SDSS-QSO. 2MPZ instead show basically no sign of ISW, which is expected given the very low z range. In the Table we also include a column with the signal to noise (S/N = A/σ_A) of the ISW measurement for comparison with other works since this quantity is often reported in the literature. We can see that the global fit reaches a S/N of 5.

We also show in Table IV the result of the fit when no redshift binning is used. It is clear that without such binning the significance of the ISW is significantly reduced, especially for SDSS-DR12 and WI × SC, while the significance of SDSS-QSO is almost unchanged. Overall, when no redshift binning is used, the significance of the ISW effect combining all the catalog is 4.0σ, which is significantly reduced with respect to the 4.7σ achieved with the redshift binning.

As mentioned above, the derived significance is very weakly dependent on the exact values of the biases used. For the case of a single catalog redshift bin, this is clear looking at Eqs. (6) and (8), which show that the ISW signal is linear in b. The fit to the cross-correlation thus constraints the quantity bA_{ISW} and the value of b is not important for the determination of the significance, although, clearly, is relevant in determining the value of A_{ISW}. When several redshift bins and catalogs are used, the above argument is not exact anymore, but remains approximately valid. We checked, indeed, that using different biases derived from the autocorrelation fits using different ℓ_{max} and different number of ℓ bins, gives unchanged significances.

We can see that the preferred A_{ISW} value from the combined fit is slightly larger than 1 at a bit more than 1σ. In the single catalog fits, both NVSS, QSOs and SDSS seem to drive the A_{ISW} value above 1. This is confirmed in the last 5 rows of Table III where different fits are performed each time excluding only one catalog and combining the remaining four. All the fits give compatible results with A_{ISW} above 1 at around 1σ or a bit more. This result is further scrutinized in Section IX where we

TABLE III.   Summary of the measured ISW and related significances for the single redshift bins of each catalogs (top table) and for various combinations of the catalogs, where, in the latter case, also the individual redshift bins of each catalog were combined (bottom table). The last five rows give the cases in which a single catalog is excluded from the fit each time. The χ^2 refers to the case of a fit with 4 bins in the multipole range 4-100.

Catalog	z	A_{ISW}	$\frac{A}{\sigma_A}$	χ_0^2	$\chi_{\min}^2$	$\Delta\chi^2$
SDSS	0–0.1	0.23 ± 3.35	0.07	1.224	1.219	0.005
	0.1–0.3	0.90 ± 1.03	0.87	3.89	3.12	0.76
	0.3–0.4	1.94 ± 1.24	1.57	4.47	2.01	2.45
	0.4–0.5	2.77 ± 1.36	2.03	6.57	2.45	4.12
	0.5–0.7	2.59 ± 1.13	2.28	9.28	4.06	5.22
	0.7–1	1.00 ± 2.72	0.37	6.76	6.62	0.13
WIxSC	0–0.09	5.24 ± 4.86	1.08	2.84	1.68	1.16
	0.09–0.21	0.34 ± 1.01	0.33	4.63	4.52	0.11
	0.21–0.3	1.04 ± 0.94	1.1	3.62	2.4	1.21
	0.3–0.6	1.33 ± 0.94	1.41	4.91	2.92	1.99
QSO	0–1	2.50 ± 1.64	1.52	5.95	3.64	2.31
	0.5–1	2.39 ± 1.65	1.45	7.46	5.34	2.11
	1–2	2.49 ± 1.64	1.52	3.99	1.68	2.31
	2–3	1.83 ± 4.80	0.38	3.11	2.96	0.14
2MPZ	0–0.105	1.25 ± 3.43	0.36	1.26	1.13	0.13
	0.105–0.195	0.53 ± 1.77	0.3	1.12	1.03	0.09
	0.195–0.3	1.04 ± 1.47	0.71	1.66	1.16	0.5
NVSS	0–6	1.70 ± 0.57	2.97	14.9	6.11	8.79

Catalog	A_{ISW}	$\frac{A}{\sigma_A}$	χ_0^2	$\chi_{\min}^2$	$\Delta\chi^2$
SDSS	1.89 ± 0.57	3.29	30.96	20.11	8.46
WIxSC	0.93 ± 0.56	1.67	13.16	10.39	2.76
Quasars	2.41 ± 1.13	2.13	14.55	10.01	2.99
2MPZ	0.87 ± 1.07	0.81	4.04	3.38	0.65
SDSS + WIxSC	1.39 ± 0.40	3.49	44.12	31.94	11.21
SDSS + Quasars	1.99 ± 0.51	3.9	45.51	30.28	11.45
SDSS + WIxSC + Quasars	1.51 ± 0.38	4	58.67	42.66	14.2
SDSS + WIxSC + Quasars + NVSS + 2MPZ	1.51 ± 0.30	5	77.61	52.61	22.16
SDSS + WIxSC + Quasars + NVSS	1.56 ± 0.31	4.97	73.57	48.85	21.52
SDSS + WIxSC + NVSS + 2MPZ	1.44 ± 0.31	4.6	63.06	41.92	19.17
SDSS + Quasars + NVSS + 2MPZ	1.75 ± 0.36	4.88	64.45	40.67	19.41
SDSS + WIxSC + Quasars + 2MPZ	1.44 ± 0.36	4.04	62.71	46.35	14.85
WIxSC + Quasars + NVSS + 2MPZ	1.36 ± 0.35	3.84	46.65	31.9	13.71

TABLE IV.   Summary of the measured ISW and related significances for the case of no redshift binning of the catalogs. Various combinations of the catalogs are shown.

Catalog	A_{ISW}	$\frac{A}{\sigma_A}$	χ_0^2	$\chi_{\min}^2$	$\Delta\chi^2$
SDSS	0.96 ± 0.65	1.49	5.3	3.09	2.21
WIxSC	0.62 ± 0.61	1.02	5.28	4.24	0.65
Quasars	1.28 ± 0.63	2.03	5.55	1.41	3.94
2MPZ	0.90 ± 2.32	0.39	0.87	0.72	0.15
NVSS	1.70 ± 0.57	2.97	14.9	6.11	8.79
SDSS + WIxSC	0.94 ± 0.42	2.23	18.47	13.48	4.96
SDSS + Quasars	1.32 ± 0.56	2.35	19.85	14.33	5.2
SDSS + WIxSC + Quasars	1.12 ± 0.40	2.84	33.02	24.97	7.95
SDSS + WIxSC + Quasars + NVSS	1.31 ± 0.33	4.02	47.91	31.76	15.27
SDSS + WIxSC + Quasars + NVSS + 2MPZ	1.27 ± 0.31	4.08	51.95	35.28	15.92

investigate if this slight difference of A_{ISW} from 1 can be interpreted as an indication of departure of DE from the simple case of a cosmological constant.

B. Method 2

The first method is, in principle, not fully self-consistent, because the auto-correlations, and hence the biases, are sensitive to the underlying matter power spectrum. We fixed the matter power spectrum to the Planck ΛCDM best-fitting model, but this may not be the best fit to the auto-correlation data. The induced error should be negligible when CMB and BAO are also used, since they impose $P(k)$ to be very close to the fiducial model. But more importantly, the cross-correlation determines a given amount of ISW, and this has in principle an effect on cosmology, since a different ISW means a different dark energy model and thus also a different $P(k)$. For these reasons it is more consistent to fit to the data at the same time as the bias parameters, the cosmological parameters, and the A_{ISW} parameter used to assess the detection significance.

We perform such a fit using the MONTEPYTHON environment. The fit typically involves many parameters (>15) which can present degeneracies which are not known in advance. To scan efficiently this parameter space we run MONTEPYTHON in the Multinest mode [75]. In this way we can robustly explore the posterior with typically $\sim 10^6$ likelihood evaluations, and efficiencies of the order of 10%. We consider two cases.

In the first case, we only use cross-correlation and auto-correlation measurements. We call this data set AC + CC, and we fit a total of 22 parameters, i.e, 15 biases, A_{ISW}, and the six ΛCDM parameters (ω_b, ω_{cdm}, n_s, h, A_s, τ_{reio}). When Planck data are used, we also include the nuisance parameter A_{Planck} [1]. For all cosmological parameters except ω_{cdm}, we use Gaussian priors derived from a fit of Planck + BAO summarized in Table V, which are consistent with those published in [1]. The error bars from Planck + BAO are so small that we find essentially the

same result for A_{ISW} when fixing these five parameters to their best fit values instead of marginalizing over them with Gaussian priors. Our results for this fit are shown in the first column of Table VI. As expected, the constraint on ω_{cdm} coming from the AC + CC data is weaker than that from Planck + BAO data, by about a factor 6. Also, the ω_{cdm} best-fit of the AC + CC analysis is lower than the Planck + BAO fit, by about 2σ. The fitted galaxy biases are typically compatible with those of Method 1, although in several cases they are 10-20% larger, which can be understood as a

TABLE VI. Result of the MONTEPYTHON fits in the ΛCDM model with using several combinations of Planck data, AC data and CC data. When the Planck data is not used, Gaussian priors on the cosmological parameters except ω_{cdm} are assumed. Here Ω_Λ is a derived parameter. The third to last row gives the Test Statistics (TS) which is equal to $\Delta\chi^2$ for the fit in the first two column and $-2\Delta\log\mathcal{L}$ for the fit in the third column. The second to last row gives the significance $\sigma = \sqrt{TS}$. Finally, the last row gives the logarithm of the Bayes factor, representing the evidence for nonzero A_{ISW} in Bayesian terms.

Parameter	AC + CC	CC	PL + AC + CC
$10^{-2}\omega_b$	2.230 ± 0.014	2.229 ± 0.013	2.228 ± 0.020
ω_{cdm}	0.1060 ± 0.0062	$0.1045^{+0.0093}_{-0.023}$	0.1185 ± 0.0012
n_s	0.9670 ± 0.0039	0.9667 ± 0.0036	0.9678 ± 0.0043
$10^{-9}A_s$	2.132 ± 0.049	2.142 ± 0.044	2.149 ± 0.051
h	0.6770 ± 0.0044	0.6775 ± 0.0044	0.6790 ± 0.0053
τ_{reio}	$\cdots$	$\cdots$	0.068 ± 0.013
$10^{-2}A_{\mathrm{Planck}}$	$\cdots$	$\cdots$	100.01 ± 0.25
A_{ISW}	1.53 ± 0.29	1.57 ± 0.29	1.62 ± 0.30
$b_{0,\mathrm{2MPZ}}$	1.276 ± 0.059	$1.37^{+0.29}_{-0.24}$	1.194 ± 0.028
$b_{1,\mathrm{2MPZ}}$	1.243 ± 0.049	$1.31^{+0.22}_{-0.31}$	1.188 ± 0.030
$b_{2,\mathrm{2MPZ}}$	1.795 ± 0.080	1.89 ± 0.27	1.743 ± 0.070
$b_{0,\mathrm{SDSS}}$	1.104 ± 0.043	$1.11^{+0.15}_{-0.24}$	1.060 ± 0.030
$b_{1,\mathrm{SDSS}}$	0.904 ± 0.030	$0.887^{+0.11}_{-0.089}$	0.883 ± 0.025
$b_{2,\mathrm{SDSS}}$	0.820 ± 0.027	$0.84^{+0.21}_{-0.13}$	0.800 ± 0.023
$b_{3,\mathrm{SDSS}}$	1.178 ± 0.038	$1.11^{+0.22}_{-0.14}$	1.160 ± 0.034
$b_{4,\mathrm{SDSS}}$	$1.12^{+0.12}_{-0.11}$	$0.99^{+0.22}_{-0.25}$	$1.11^{+0.12}_{-0.10}$
$b_{0,\mathrm{WISC}}$	0.951 ± 0.040	$1.01^{+0.15}_{-0.23}$	0.914 ± 0.030
$b_{1,\mathrm{WISC}}$	0.851 ± 0.032	$0.85^{+0.16}_{-0.21}$	0.828 ± 0.026
$b_{2,\mathrm{WISC}}$	1.005 ± 0.038	$0.99^{+0.16}_{-0.20}$	0.988 ± 0.034
$b_{0,\mathrm{QSO}}$	$1.44^{+0.25}_{-0.22}$	$1.26^{+0.45}_{-0.32}$	$1.40^{+0.27}_{-0.22}$
$b_{1,\mathrm{QSO}}$	$2.46^{+0.26}_{-0.22}$	$1.90^{+0.60}_{-0.41}$	$2.47^{+0.27}_{-0.24}$
$b_{2,\mathrm{QSO}}$	$3.35^{+0.41}_{-0.33}$	$2.68^{0.60}_{-0.52}$	$3.34^{+0.46}_{-0.39}$
b_{NVSS}	2.54 ± 0.11	2.31 ± 0.39	2.479 ± 0.097
Ω_Λ	0.720 ± 0.014	$0.722^{+0.050}_{-0.022}$	0.694 ± 0.005
TS	22.0	26.5	24.9
σ	4.7	5.1	5.0
$\Delta\log(\mathrm{ev})$	11.9	11.5	12.7

TABLE V. Results of the MONTEPYTHON fit to Planck + BAO data only. Here Ω_Λ is a derived parameter and A_{Planck} a Planck nuisance parameter.

Parameter	68% limits
$10^{-2}\omega_b$	2.226 ± 0.019
ω_{cdm}	0.1187 ± 0.0012
n_s	0.9674 ± 0.0043
$10^{-9}A_s$	2.152 ± 0.052
h	0.6780 ± 0.0053
τ_{reio}	0.068 ± 0.013
$10^{-2}A_{\mathrm{Planck}}$	100.01 ± 0.25
Ω_Λ	0.6916 ± 0.0071

consequence of the lower ω_{cdm}, resulting in a lower $P(k)$ normalization. Indeed, the measured auto-correlations basically fix the product of the squared biases and of the overall $P(k)$ amplitude. Comparing the case with free $A_{\rm ISW}$ to the one with $A_{\rm ISW} = 0$, we find TS $= \Delta\chi^2 = 22$, giving a significance of 4.7σ, identical to the one found in Method 1. With the same setup we also perform a fit using CC data only. The results are shown in the second column of Table VI. In this case the biases are determined from the cross-correlation only, without relying on the autocorrelation. It is interesting to see that, even in this case, good constraints on the biases can be achieved, although, clearly, the errors are much larger (by a factor of $\sim$4–5) than when including the AC data. We find for this case TS $= 26.5$ corresponding to a significance of 5.1σ, thus reaching the 5σ threshold. The increase in significance seems to be due to the larger freedom in the fit of the biases which allows to reach an overall better best-fit of the CC data with respect to the case in which the biases are constrained by the AC data.

In the second case, we fit the same parameters to the data, but we now include the full Planck + BAO likelihoods instead of Gaussian priors on five parameters. Formally, we use the Planck and BAO likelihoods combined with the χ^2 from the AC + CC data:

$$\log L = \log L_{\rm PL} + \log L_{\rm BAO} - \chi^2_{AC}/2 - \chi^2_{CC}/2. \quad (10)$$

It should be noted that the use of other data besides AC + CC does not affect the ability to derive the significance of the ISW detection, which is only encoded in the parameter $A_{\rm ISW}$ entering the AC + CC likelihood. Results of this fit are shown in the third column of Table VI. The main difference with respect to the previous fit is the value of ω_{cdm}, now driven back to the Planck best-fit. This upward shift in ω_{cdm} results, again, in a global downward shift of the biases, by about 10–20%, giving now a better compatibility with the results of Method 1.

In general, apart from the small degeneracy with ω_{cdm} resolved by the inclusion of Planck + BAO data, the biases are well constrained by the fit. This means that the sub-space of biases is approximately orthogonal to the rest of the global parameter space, which simplifies the fit and speeds up its convergence. To measure the significance, in this case we define the test statistic as TS $= -2\Delta\log\mathcal{L}$, which shares the same properties of the TS defined in terms of the χ^2. Comparing the case with free $A_{\rm ISW}$ to the one with $A_{\rm ISW} = 0$, we now get TS $= -2\Delta\log\mathcal{L} = 24.9$, which gives a significance of 5.0σ. Since the cosmology is basically fixed by the Planck + BAO data to a point in parameter space very close to the fiducial model of Method 1, this improvement in significance comes, apparently, from fitting jointly the biases and $A_{\rm ISW}$ (while in Method 1 the biases were kept

fixed using the results of the first step of the method). The joint fit explores the correlations which exist between the biases and $A_{\rm ISW}$. This results in a better global fit, and also in a slightly enhanced $A_{\rm ISW}$ significance, reaching the 5σ threshold.

Finally, since the fit performed with Multinest automatically provides also the *evidence* of the Posterior, in the last row of Table VI we additionally report the logarithm of the Bayes factor, i.e., the logarithm of the ratio of the evidences for the two fits where $A_{\rm ISW}$ is free and where it is fixed to $A_{\rm ISW} = 0$. We find in all cases values around $\sim$12. Logarithm of the Bayes factors larger than 5 represents *strong evidence* according to Jeffreys' scale [76].

VIII. ROBUSTNESS TESTS

In this section we describe some further tests performed to verify the robustness of the results.

As mentioned in Sec. III, several CMB maps are available from Planck, resulting from different foreground cleaning methods. In Fig. 3 we show the results of the cross-correlation using four CMB maps cleaned with four different methods. We pick up as an example the cross-correlation with the full 2MPZ catalog, without subdivision in redshift bins. It clearly appears that the use of different maps has no appreciable impact on the result.

Another important aspect is the possible frequency dependence of the correlation. In particular, while the ISW effect is expected to be achromatic, some secondary effects, like a correlation due to a Sunyaev-Zel'dovich [77] or Rees-Sciama [78] imprint in the CMB map, are expected to be frequency dependent. To test this possibility, we use available Planck CMB maps at 100 GHz, 143 GHz and 217 GHz. Again the full 2MPZ catalog is used as example,
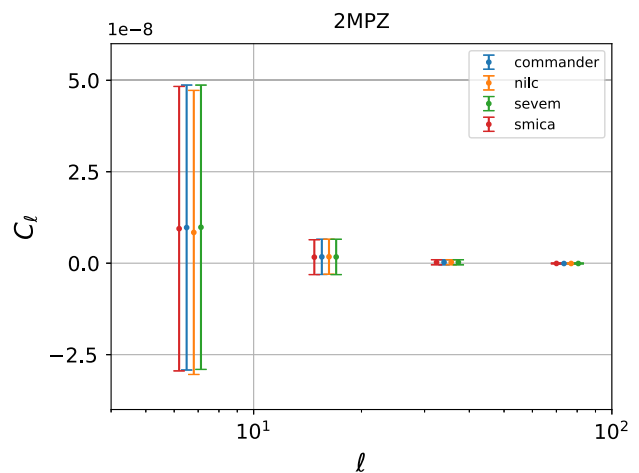

FIG. 3. Measured cross-correlation of 2MPZ in one single redshift bin with CMB maps from Commander, NILC, SEVEM, and SMICA.
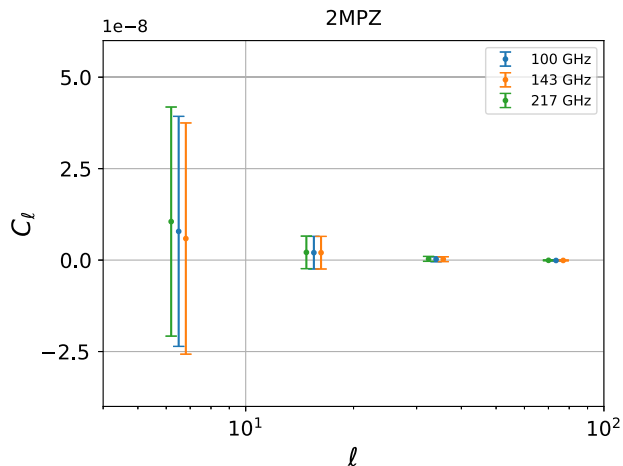
FIG. 4. Measured cross-correlation of 2MPZ in one single redshift bin with CMB at 100 GHz, 143 GHz and 217 GHz.

since these effects are expected to peak at low redshift. Fig. 4 shows the result of the correlation at different frequencies. We observe a very small trend of the CAPS with frequency, especially for the first ℓ bin, but this effect is negligible with respect to the error bars of the data points. Results are similar for the other catalogs, showing no frequency dependence.

Finally, we tested the effect of photo-z errors. In the basic setup, the theoretical predictions for the auto- and cross-correlation functions per redshift bin are modeled by assuming that the true redshift distribution is well approximated by the photo-z one, i.e. $dN/dz_{\text{true}} \simeq dN/dz_{\text{phot}}$. In reality, sharp cuts in dN/dz_{phot} will correspond to more extended tails in dN/dz_{true} because the photo-zs are smeared out in the radial direction. However, we can easily take photo-z errors into account if we know their statistical properties. In the case of 2MPZ, the photo-z error is basically constant in z and has roughly Gaussian scatter of $\sigma_{\delta z} \simeq 0.015$ centered at $\langle \delta z \rangle = 0$, while for WI × SC the scatter is $\sigma_{\delta z}(z) = 0.033(1 + z)$ with also approximately zero mean in δz. For SDSS QSOs it is also approximately constant in z and equal to 0.24. Finally, for SDSS DR12 the error is $\sigma_{\delta z}(z) = 0.022(1 + z)$ (see Sec. V). We thus derive the effective true redshift distribution of a given bin by convolving the measured photo-z selection function in that bin with a z-dependent Gaussian of width $\sigma_{\delta z}(z)$. The resulting true-z distribution is a smoothed version of the photo-z distribution, presenting tails outside the edges of the bin. We then use this distribution to fit again the auto- and cross-correlations data. The results are shown in the last column of Table II. We find that the effect of photo-z errors has some impact on the determination of the biases. The effect is most important in the high-z tails of various catalogs, and, in particular, WI × SC and SDSS DR12. This is not surprising since, in these cases, the photo-z errors increase with redshift and are largest at high-z. The effect is

at the level of 10–20%. This corresponds to a decrease in A_{ISW} of the same amount in these bins. Nonetheless, since the above bins only have a limited weight on the combined fit, the impact on the final A_{ISW} determined from the global fit of all bins and catalogs is basically negligible.

IX. DARK ENERGY FIT

In this section we investigate the power of the cross-correlation data to constrain DE, in a similar framework as presented in [79,80,81]. For this purpose, we do not use the A_{ISW} parameter employed in Sec. VII, since it is only an artificial quantity necessary to evaluate the ISW significance from the cross-correlation data. However, as shown in Sec. VII, there is indication that the best-fit value of A_{ISW} is above 1 at slightly more than 1σ. This suggests (although with low statistical significance) that DE could differ from a simple cosmological constant. To investigate this more in detail, we perform a fit with Method 2 of Sec. VII, but with $A_{\text{ISW}} = 1$, and with extra parameters accounting for dynamical dark energy. For simplicity, we use the $w_0 - w_a$ empirical parametrization [82,83] and the parameterized post-Friedmann framework of [84,85], which are implemented in CLASS, to study models with $w < -1$. We test several different fit setups. In particular, since the AC data set is a cosmological probe with its own sensitivity to the cosmological parameters, we test various combinations in which the AC and CC data are used separately. A further reason to study the AC data separately from the CC ones is that the APS of extragalactic objects are typically difficult to model accurately, even at small ℓ, due to the nonlinearity and possible stochasticity of the galaxy bias with respect to matter. Separate fits to the AC and CC data could then reveal inconsistencies that might be associated to our minimal assumption that the bias is linear and scale-independent. A further reason to study separately the AC and CC data is the fact that the AC ones are more prone to possible systematic effects present in the catalogs like, for example, nonuniform calibration across the sky. These systematics would more severely bias the AC-based

TABLE VII. Results of the MONTEPYTHON fit with using Planck + BAO data.

Parameter	68% limits
$10^{-2}\omega_b$	2.224 ± 0.021
ω_{cdm}	0.1190 ± 0.0017
n_s	0.9668 ± 0.0051
$10^{-9}A_s$	2.137 ± 0.063
h	$0.639^{+0.018}_{-0.029}$
w_0	$-0.58^{+0.30}_{-0.25}$
w_a	-1.10 ± 0.76
$\Omega_{0,fld}$	$0.650^{+0.024}_{-0.029}$

cosmological inference, while the CC measurements are more robust in this respect, since systematic offsets or miscalibrations across the sky do not generally correlate with the LSS nor the CMB.

We perform the following fits: (a) Planck + BAO, (b) Planck+BAO+CC+AC, (c) Planck + BAO + CC, (d) CC only, (e) AC only, (f) AC + CC. Case (a) has the standard 6 ΛCDM parameters, plus w_a, w_0, and one Planck nuisance parameter, A_{Planck}, required for the evaluation of the Planck likelihood [1], thus 9 parameters in total. The results of this baseline fit are shown in Table VII. Case (b) includes CC and AC data sets and uses additionally 15 bias parameters (24 parameters in total). Case (c) is similar to (b) but without AC data. Since the biases are still needed for the CC fitting, they are still included in the fit, but with a Gaussian prior coming from fit (b). We verified that just fixing the biases to the best fit (b), instead of including them in the fit with Gaussian priors, does not actually change the results. Similarly, the result does not change if the biases are taken from another fit than (b), like (e) or (f). For fit (d), featuring only CC data, all cosmological parameters except (w_a, w_0, ω_{cdm}) and all bias parameters are either fixed or marginalized with Gaussian priors. For fit (e), featuring only AC data, all cosmological parameters except (w_a, w_0, ω_{cdm}) are fixed to best-fit values, while the biases are left free, since they are constrained by the AC data. Finally fit (f) combines AC and CC data, and uses the same setup as fit (e).

Figures 5–6 show the results for w_0 and w_a (marginalized over all the remaining parameters) for some of these fits.
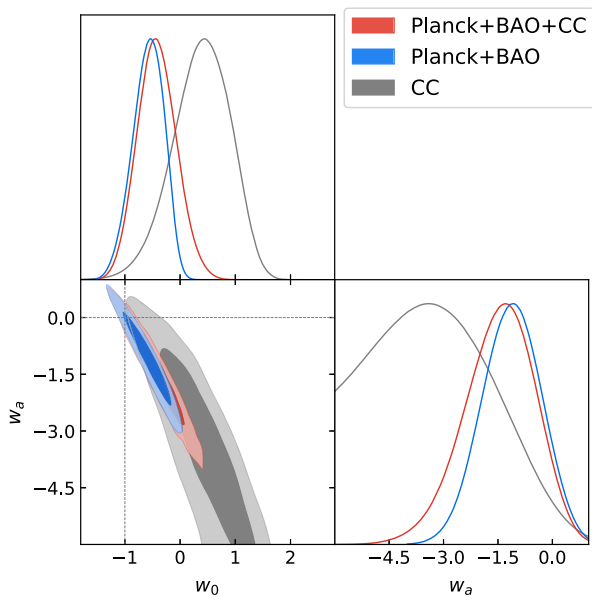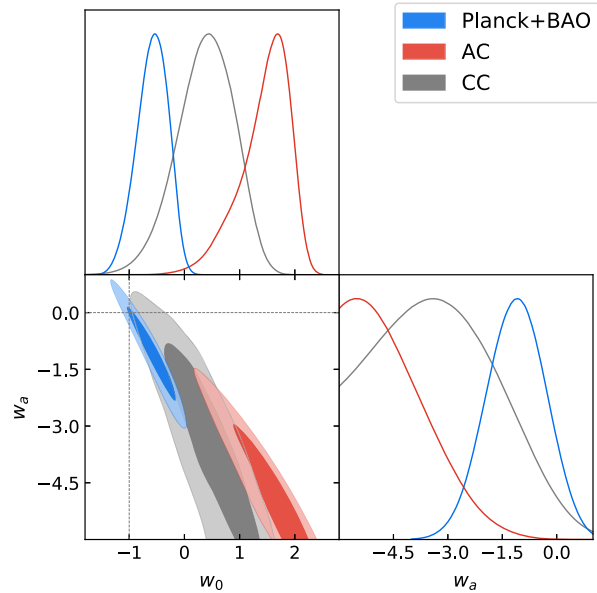
FIG. 6. Marginalized posterior in the $w_0 - w_a$ plane for the three different fits, Planck + BAO, CC only, and AC only.

Table VIII gives the confidence intervals on all the parameters for all our fits. The most evident result is that the AC-only fit selects a region of parameter space significantly in tension with the Planck + BAO constraints, basically excluding the standard case (w_0, w_a) = (−1, 0) at more than 3σ. This is either a consequence of the linear bias model not being accurate enough to provide reliable cosmological constraints, or an indication of some systematic effects in some of the catalogs. Problems in the modeling of the bias might be particularly relevant for the auto-correlation of the catalogs in the highest redshift bins, which are the most sensitive to deviations from a standard cosmological constant, but also the ones lying in the tail of the redshift distribution of the catalog, where different population of galaxies are probably selected, which requires more accurate modeling. More sophisticated approach to the modeling of the catalog auto-correlations might be thus required to address properly this issue. Various bias models have been proposed beyond linear bias, like for instance models based on the halo occupation distribution of the catalog objects (see for instance [86]). We leave a systematic study of this subject for future work. Intrinsic artifacts in the catalog, like nonuniformity in the sky coverage, or large errors in the photo-z determination, are also a likely issue. These problems can become more evident especially in the tails of the redshift distribution. Indeed, the largest χ^2 for AC fits from Table II are for the z-bins in the tail of the distribution, especially for SDSS DR12 and QSOs, indicating a poor match between the model and the data. This can be seen more explicitly also in the related plots in Appendix.

FIG. 5. Marginalized posterior in the $w_0 - w_a$ plane for the three different fits, Planck + BAO, Planck + BAO + CC and CC only.

TABLE VIII.   Result of the MONTEPYTHON fits in the ΛCDM $+ w_0 + w_a$ model with using several combinations of Planck $+$ BAO (PL) data, AC data and CC data. When the Planck data is not used, Gaussian priors on all cosmological parameters except (ω_{cdm}, w_0, w_a) are assumed.

Parameter	AC + CC	CC + bias priors	AC	PL + AC + CC	PL + CC + bias priors
$10^{-2}\omega_b$	2.222 ± 0.021	2.222 ± 0.022	2.222 ± 0.021	2.232 ± 0.022	2.227 ± 0.022
ω_{cdm}	0.1134 ± 0.0075	$0.111^{+0.016}_{-0.029}$	0.114 ± 0.011	0.1179 ± 0.0018	0.1185 ± 0.0018
n_s	0.9652 ± 0.0055	0.9642 ± 0.0057	0.9647 ± 0.0055	0.9691 ± 0.0056	0.9681 ± 0.0054
$10^{-9}A_s$	2.162 ± 0.076	2.187 ± 0.080	2.183 ± 0.077	2.151 ± 0.065	2.152 ± 0.064
h	$0.624^{+0.023}_{-0.029}$	0.641 ± 0.031	0.592 ± 0.058	$0.625^{+0.026}_{-0.030}$	$0.625^{+0.028}_{-0.031}$
τ_{reio}	$\cdots$	$\cdots$	$\cdots$	0.069 ± 0.017	0.068 ± 0.016
Ω_Λ	0.650 ± 0.029	$0.672^{+0.068}_{-0.048}$	$0.605^{+0.069}_{-0.049}$	0.639 ± 0.038	$0.635^{+0.037}_{-0.032}$
w_0	$0.97^{+0.57}_{-0.44}$	$0.39^{+0.57}_{-0.46}$	$1.46^{+0.55}_{-0.27}$	-0.37 ± 0.33	$-0.43^{+0.32}_{-0.36}$
w_a	$-3.6^{+1.2}_{-1.5}$	$-3.2^{+1.4}_{-1.9}$	$-4.47^{+0.59}_{-1.4}$	$-1.63^{+1.0}_{-0.86}$	$-1.44^{+1.0}_{-0.81}$
$10^{-2}A_{Planck}$	$\cdots$	$\cdots$	$\cdots$	100.02 ± 0.25	100.02 ± 0.25
$b_{0,2MPZ}$	$1.56^{+0.13}_{-0.12}$	$1.2220^{+0.0073}_{-0.021}$	$1.68^{+0.11}_{-0.042}$	1.240 ± 0.040	$1.2220^{+0.0076}_{-0.021}$
$b_{1,2MPZ}$	1.46 ± 0.11	1.188 ± 0.030	$1.56^{+0.10}_{-0.056}$	1.228 ± 0.041	1.188 ± 0.030
$b_{2,2MPZ}$	1.94 ± 0.15	1.743 ± 0.070	$2.04^{+0.14}_{-0.11}$	1.773 ± 0.076	1.744 ± 0.069
$b_{0,SDSS}$	1.195 ± 0.090	1.060 ± 0.030	$1.254^{+0.081}_{-0.056}$	1.078 ± 0.033	1.060 ± 0.030
$b_{1,SDSS}$	$0.861^{+0.065}_{-0.086}$	0.882 ± 0.030	$0.879^{+0.057}_{-0.065}$	0.880 ± 0.027	0.884 ± 0.030
$b_{2,SDSS}$	$0.743^{+0.057}_{-0.082}$	0.800 ± 0.025	$0.747^{+0.052}_{-0.065}$	0.792 ± 0.024	0.801 ± 0.025
$b_{3,SDSS}$	$1.016^{+0.074}_{-0.12}$	1.161 ± 0.035	$1.004^{+0.069}_{-0.11}$	1.141 ± 0.036	1.161 ± 0.035
$b_{4,SDSS}$	$0.935^{+0.098}_{-0.13}$	1.110 ± 0.020	$0.902^{+0.089}_{-0.13}$	$1.09^{+0.11}_{-0.10}$	1.110 ± 0.020
$b_{0,WISC}$	1.085 ± 0.083	0.913 ± 0.030	$1.155^{+0.078}_{-0.053}$	0.940 ± 0.035	0.913 ± 0.030
$b_{1,WISC}$	$0.884^{+0.068}_{-0.077}$	0.828 ± 0.030	$0.924^{+0.062}_{-0.055}$	0.840 ± 0.029	0.828 ± 0.031
$b_{2,WISC}$	$0.981^{+0.078}_{-0.097}$	0.987 ± 0.041	1.008 ± 0.070	0.990 ± 0.036	0.988 ± 0.040
$b_{0,QSO}$	1.14 ± 0.22	1.401 ± 0.030	1.10 ± 0.20	1.40 ± 0.22	1.401 ± 0.030
$b_{1,QSO}$	1.77 ± 0.26	2.470 ± 0.030	$1.67^{+0.23}_{-0.32}$	$2.44^{+0.26}_{-0.23}$	2.470 ± 0.030
$b_{2,QSO}$	$2.47^{+0.35}_{-0.40}$	3.341 ± 0.050	$2.34^{+0.27}_{-0.49}$	$3.34^{+0.41}_{-0.35}$	3.339 ± 0.049
b_{NVSS}	$2.36^{+0.17}_{-0.24}$	2.47 ± 0.10	$2.38^{+0.17}_{-0.22}$	2.484 ± 0.099	2.487 ± 0.098

Hence, in deriving DE constraints it is more conservative to discard information from AC and focus on CC only. We see that the constraints from the CC data are compatible with Planck + BAO results. However, given the relatively low significance of the ISW effect, the former are about three times weaker than the latter for each parameter. The direction of the degeneracy between w_0 and w_a is approximately the same in the two fits, which was not obvious *a priori*, since the two data sets are sensitive to dark energy through different physical effects (the ISW effect in CMB temperature angular spectrum for the CC fit, and the constraint on the BAO scale for the Planck + BAO fit). It appears that the valley of well-fitting models with $w_0 > -1$ always corresponds to $w(z)$ crossing -1 in the range $0.0 < z < 1.5$, but with very different derivatives $w'(z)$. Even when w_0 is very large, all models in this valley do feature accelerated expansion of the Universe

in the recent past, but not necessarily today. In fact, when w_0 increases while w_a decreases simultaneously, the stage of accelerated expansion is preserved but translated backward in time.

Since the CC data are less sensitive than Planck and do not feature a different direction of degeneracy, the joint constraints from Planck + BAO + CC are basically unchanged with respect to Planck + BAO only.

X. DISCUSSION AND CONCLUSIONS

We derived an updated measurement of the ISW effect through cross-correlations of the cosmic microwave background with several galaxy surveys, namely, 2MASS Photometric Redshift catalog (2MPZ), NVSS, SDSS QSOs, SDSS DR12 photometric redshift data set, and WISE × SuperCOSMOS; the two latter are here used for the first time for an ISW analysis. We also improved

with respect to previous analyses performing tomography within each catalog, i.e., exploiting the photometric redshifts and dividing each catalog into redshift bins. We found that the current cross-correlation data provide strong evidence for the ISW effect and thus for dark energy, at the 5σ level.

However, current catalogs are still not optimal to derive cosmological constraints from the ISW, for two main reasons. First, the clustering of objects requires complicated modeling, probably beyond the simple linear bias assumption. On this last point, improvements are possible using more sophisticated modeling, but at a price of introducing more nuisance parameters. Also, the tails of the redshift distributions of the objects might be more strongly affected by catalog systematics such as uneven sampling or large photo-z errors.

Second, the data used in this paper are sensitive mostly to the redshift range $0 < z < 0.6$, while the ISW effect is expected to be important for $0.3 < z < 1.5$. Several planned or forthcoming wide-angle galaxy surveys will cover this redshift range and should thus bring (major) improvement for ISW detection via cross-correlation with CMB. For the Euclid satellite, the predicted significance of such a signal is $\sim 8\sigma$ [87], and one should expect similar figures from the Large Synoptic Survey Telescope [88], and the Square-Kilometer Array [89]. The very high S/N of ISW from these deep and wide future catalogs will not only allow for much stronger constraints on dark energy than we obtained here, but even on some modified gravity models which often predict very different ISW signatures than ΛCDM [e.g. [90]].

ACKNOWLEDGMENTS

APPENDIX: AUTO- AND CROSS-CORRELATION RESULTS

In this appendix, we show the measured APS and CAPS and the related best-fit model for all the catalogs and z-bins considered in the analysis. APS plots are shown in Figs. 7,8, and 9, while CAPS plots are shown in Figs. 10, 11, and 12. Dots refer to the measured single multipoles, while data points with error bars refer to binned measurements.
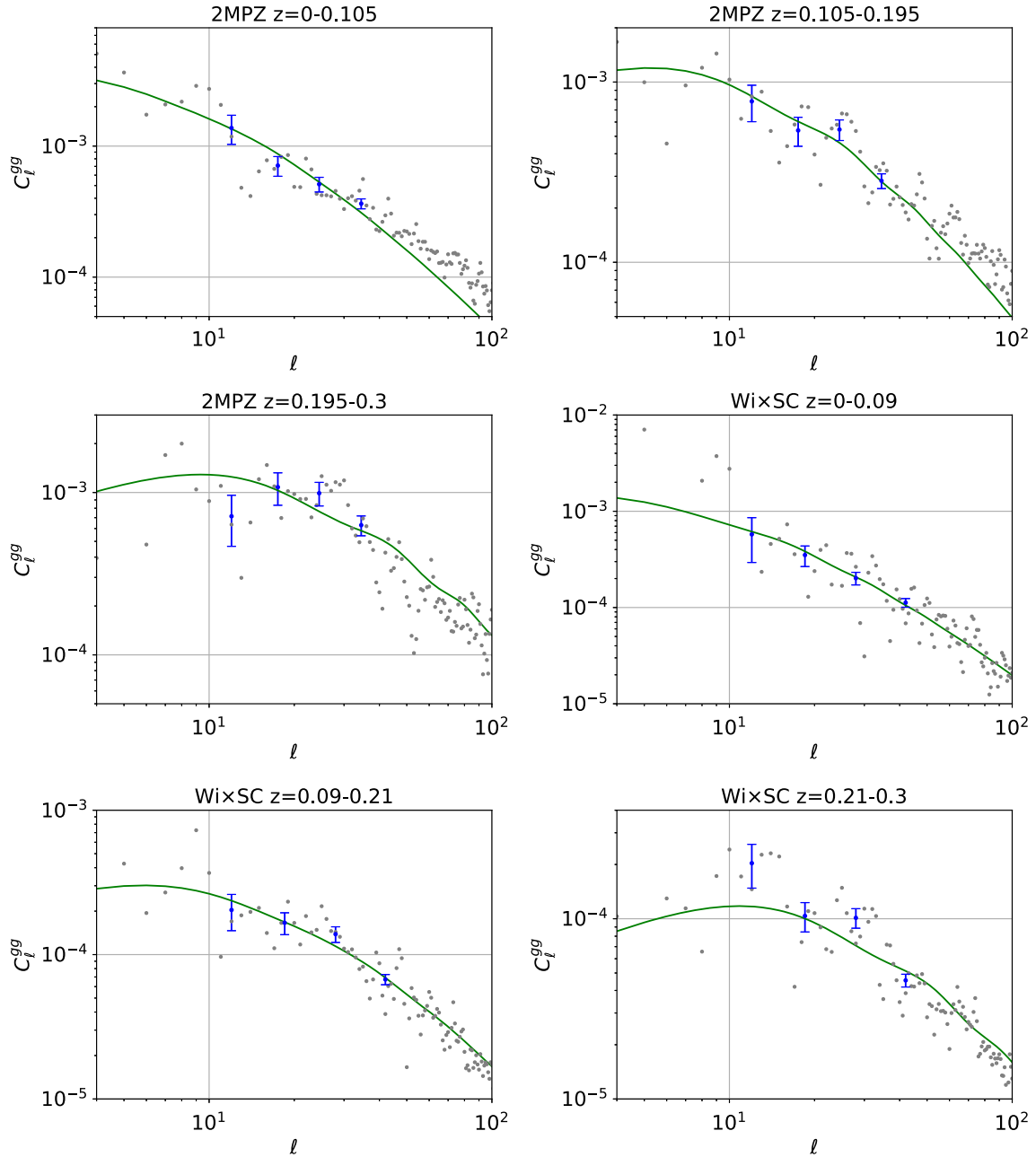

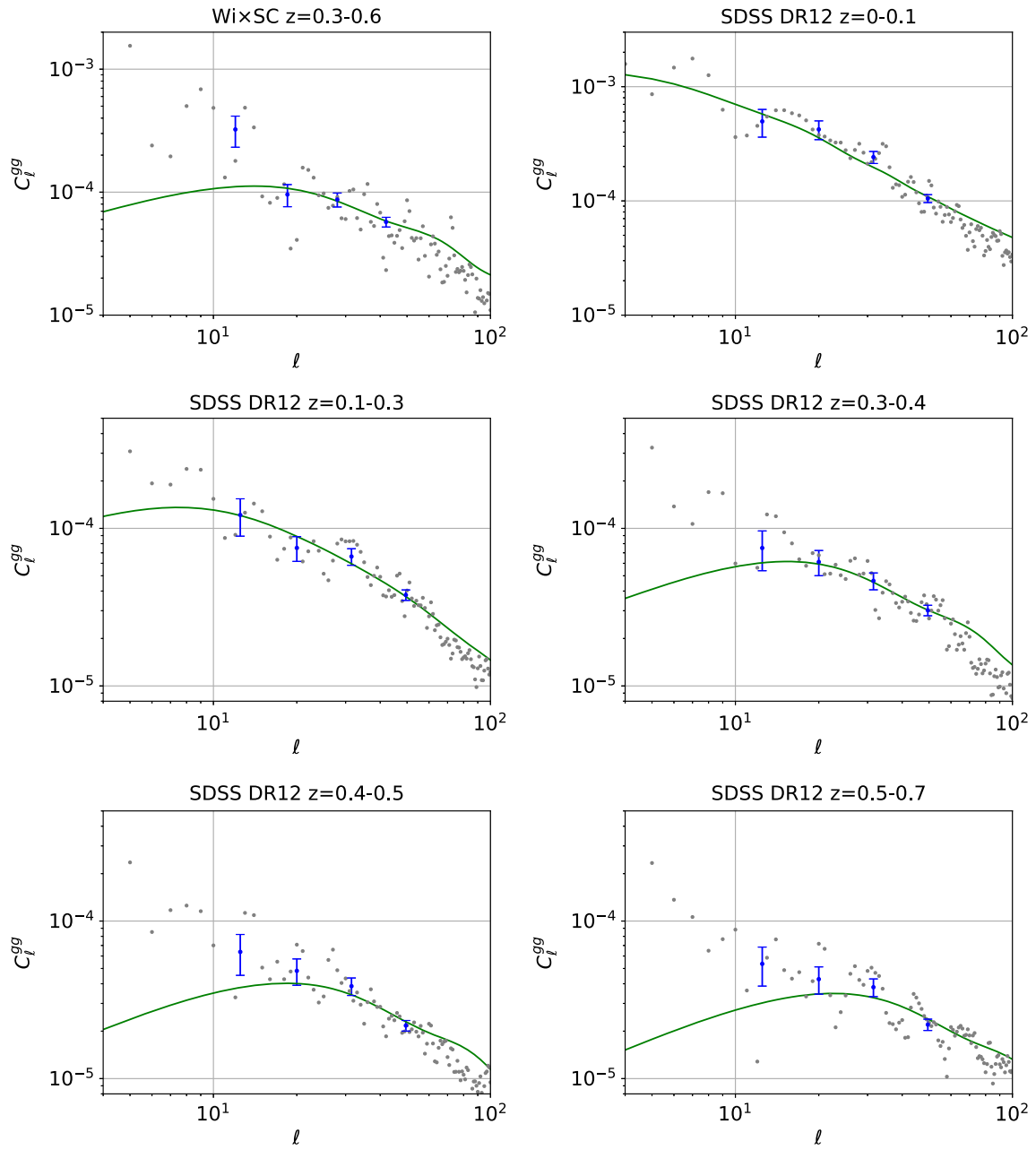FIG. 7.   Measured auto-correlation for different catalogs and redshift bins.

FIG. 8.   Measured auto-correlation for different catalogs and redshift bins.
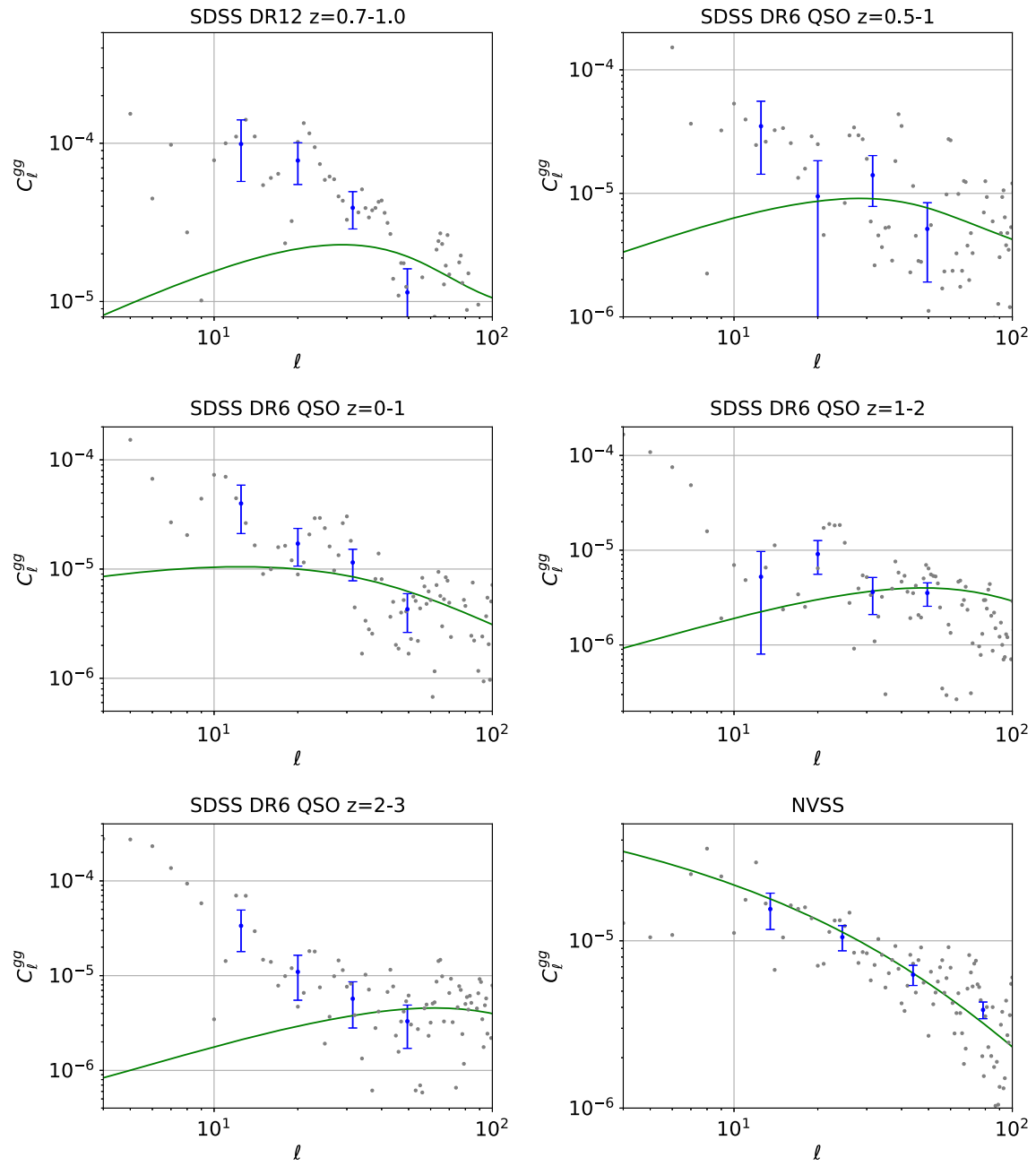
FIG. 9. Measured autocorrelation for different catalogs and redshift bins.
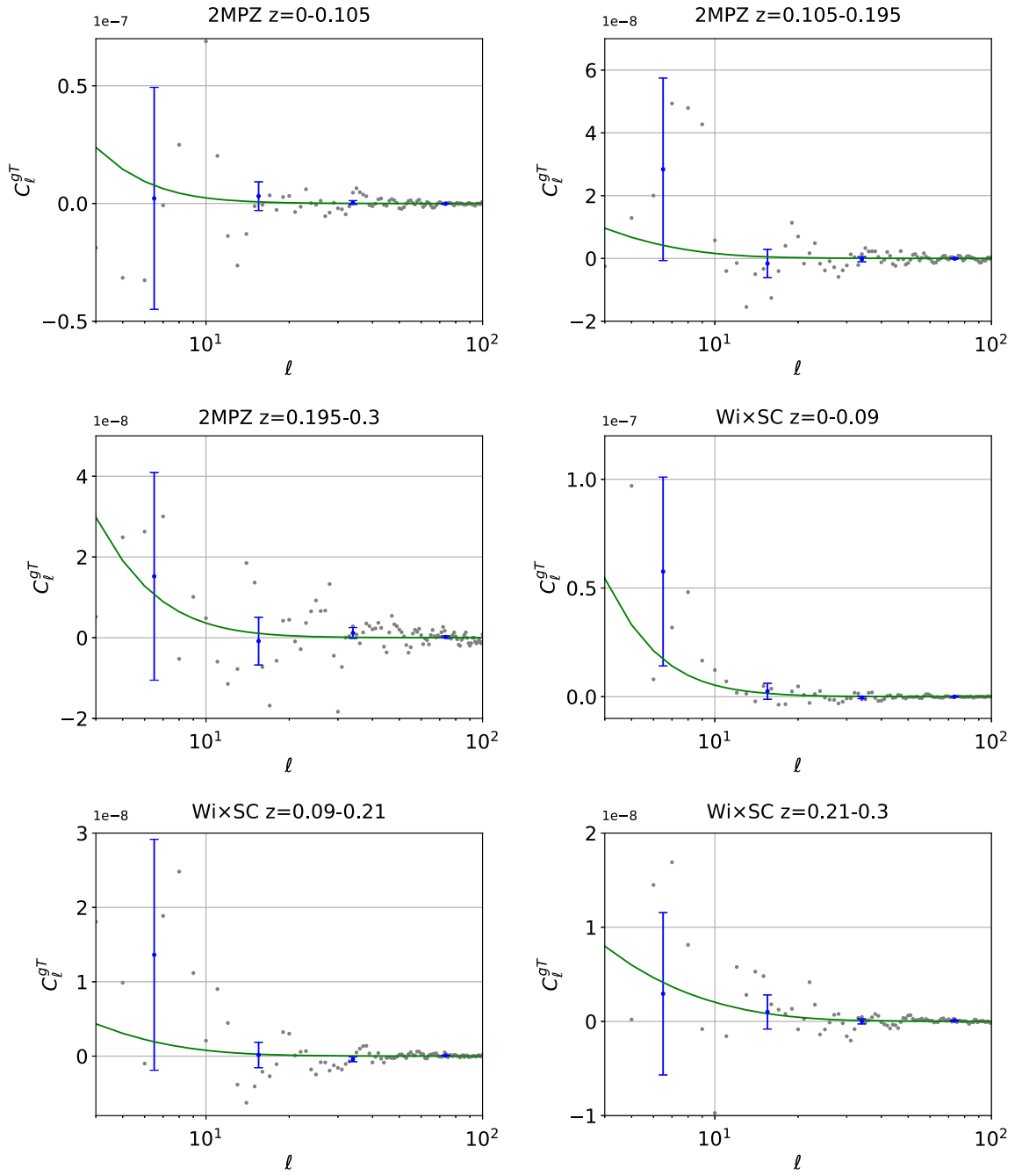
FIG. 10. Measured cross-correlation with the CMB for different catalogs and redshift bins.
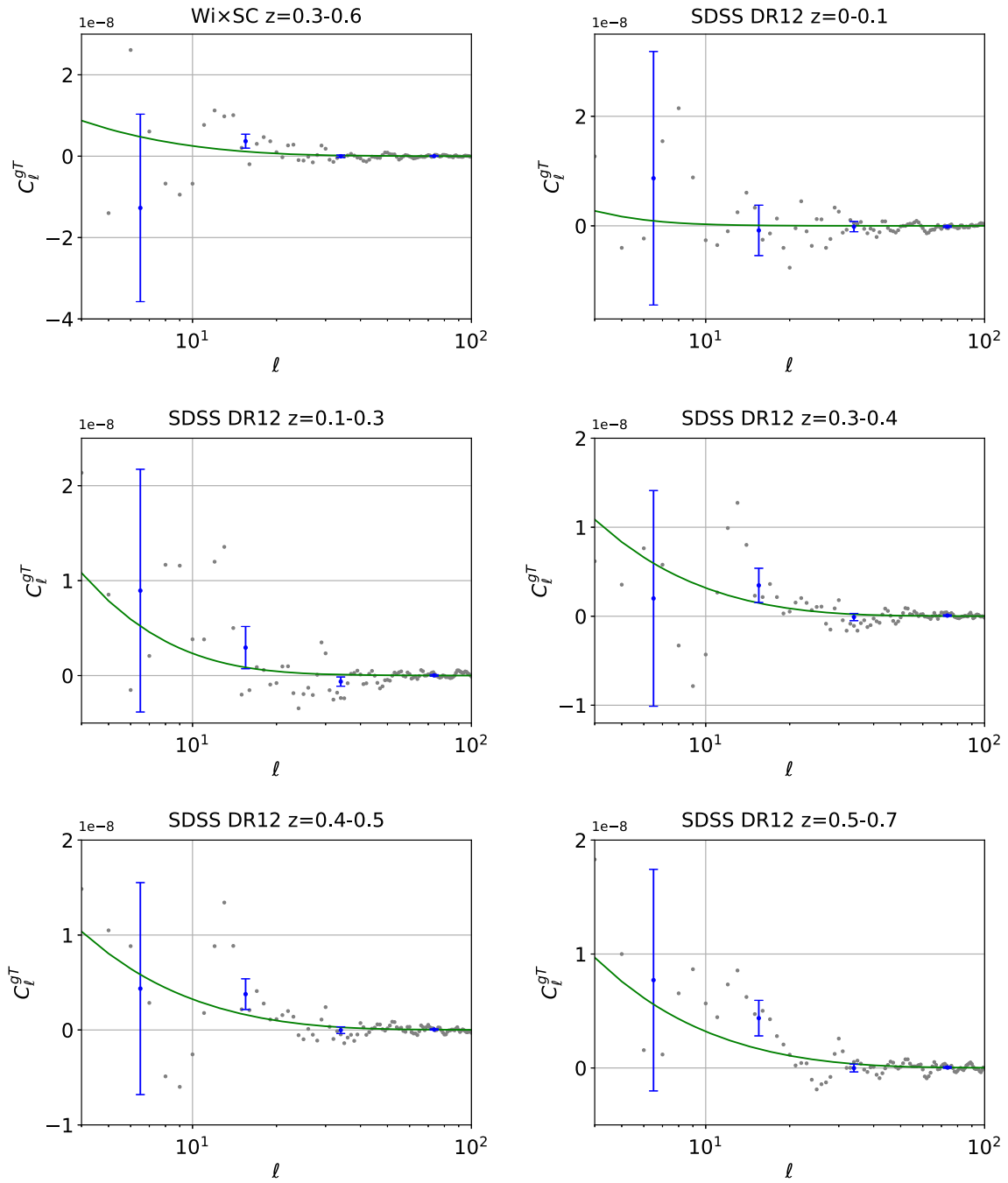
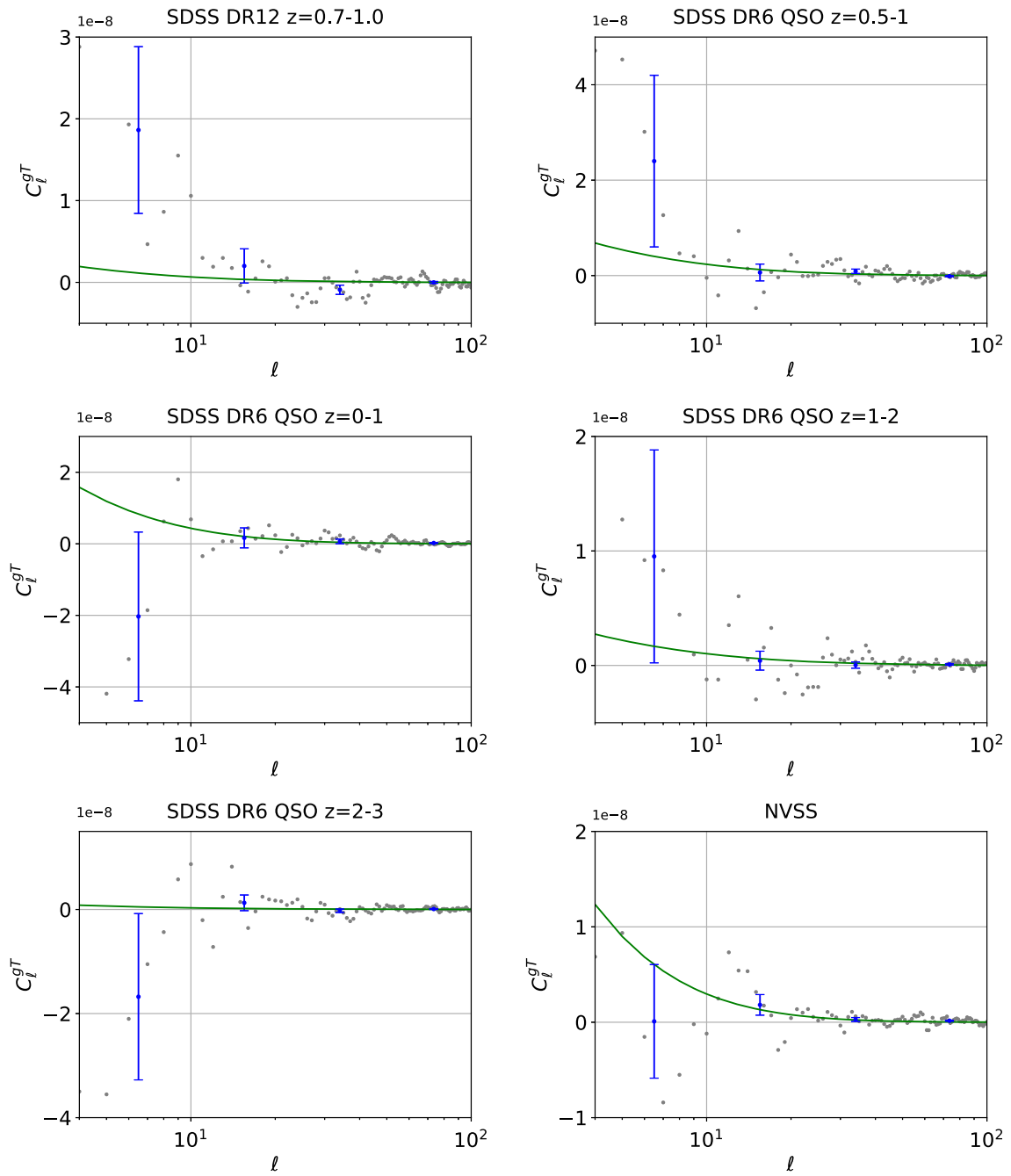FIG. 11. Measured cross-correlation with the CMB for different catalogs and redshift bins.

FIG. 12.   Measured cross-correlation with the CMB for different catalogs and redshift bins.

[1] P. A. R. Ade *et al.* (Planck Collaboration), Astron. Astrophys. **594,** A13 (2016).

[2] M. Betoule *et al.*, Astron. Astrophys. **568,** A22 (2014).

[3] R. K. Sachs and A. M. Wolfe, Astrophys. J. **147,** 73 (1967).

[4] M. Kamionkowski, Phys. Rev. D **54,** 4169 (1996).

[5] A. Kinkhabwala and M. Kamionkowski, Phys. Rev. Lett. **82,** 4172 (1999).

[6] Y.-S. Song, W. Hu, and I. Sawicki, Phys. Rev. D **75,** 044004 (2007).

[7] A. Barreira, B. Li, C. M. Baugh, and S. Pascoli, Phys. Rev. D **86,** 124016 (2012).

[8] S. P. Boughn, R. G. Crittenden, and N. G. Turok, New Astron. **3,** 275 (1998).

[9] S. P. Boughn and R. G. Crittenden, Phys. Rev. Lett. **88,** 021302 (2001).

[10] N. Afshordi, Phys. Rev. D **70,** 083536 (2004).

[11] F.-X. Dupe, A. Rassat, J.-L. Starck, and M. J. Fadili, Astron. Astrophys. **534,** A51 (2011).

[12] P. A. R. Ade *et al.* (Planck Collaboration) Astron. Astrophys. **571,** A19 (2014).

[13] P. A. R. Ade *et al.* (Planck Collaboration), Astron. Astrophys. **594,** A21 (2016).

[14] N. Afshordi, Y. Loh, and M. A. Strauss, Phys. Rev. D **69,** 083524 (2004).

[15] S. Boughn and R. Crittenden, Nature (London) **427,** 45 (2004).

[16] P. Fosalba, E. Gaztanaga, and F. Castander, Astrophys. J. **597,** L89 (2003).

[17] A. Cabré, P. Fosalba, E. Gaztañaga, and M. Manera, Mon. Not. R. Astron. Soc. **381,** 1347 (2007).

[18] A. Cabré, E. Gaztañaga, M. Manera, P. Fosalba, and F. Castander, Mon. Not. R. Astron. Soc. **372,** L23 (2006).

[19] T. Giannantonio, R. G. Crittenden, R. C. Nichol, R. Scranton, G. T. Richards, A. D. Myers, R. J. Brunner, A. G. Gray, A. J. Connolly, and D. P. Schneider, Phys. Rev. D **74,** 063520 (2006).

[20] A. Raccanelli, A. Bonaldi, M. Negrello, S. Matarrese, G. Tormen, and G. de Zotti, Mon. Not. R. Astron. Soc. **386,** 2161 (2008).

[21] A. Rassat, K. Land, O. Lahav, and F. B. Abdalla, Mon. Not. R. Astron. Soc. **377,** 1085 (2007).

[22] J. Xia, M. Viel, C. Baccigalupi, and S. Matarrese, J. Cosmol. Astropart. Phys. 9 (2009) 3.

[23] S. Ferraro, B. D. Sherwin, and D. N. Spergel, Phys. Rev. D **91,** 083533 (2015).

[24] C. Hernandez-Monteagudo *et al.*, Mon. Not. R. Astron. Soc. **438,** 1724 (2014).

[25] A. J. Shajib and E. L. Wright, Astrophys. J. **827,** 116 (2016).

[26] D. Pietrobon, A. Balbi, and D. Marinucci, Phys. Rev. D **74,** 043524 (2006).

[27] J. D. McEwen, P. Vielva, M. P. Hobson, E. Martinez-Gonzalez, and A. N. Lasenby, Mon. Not. R. Astron. Soc. **376,** 1211 (2007).

[28] P. Vielva, E. Martinez-Gonzalez, and M. Tucci, Mon. Not. R. Astron. Soc. **365,** 891 (2006).

[29] T. Giannantonio, R. Scranton, R. G. Crittenden, R. C. Nichol, S. P. Boughn, A. D. Myers, and G. T. Richards, Phys. Rev. D **77,** 123520 (2008).

[30] T. Giannantonio, R. Crittenden, R. Nichol, and A. J. Ross, Mon. Not. R. Astron. Soc. **426,** 2581 (2012).

[31] S. Ho, C. Hirata, N. Padmanabhan, U. Seljak, and N. Bahcall, Phys. Rev. D **78,** 043519 (2008).

[32] B. R. Granett, M. C. Neyrinck, and I. Szapudi, Astrophys. J. **683,** L99 (2008).

[33] P. Pápai, I. Szapudi, and B. R. Granett, Astrophys. J. **732,** 27 (2011).

[34] S. Ilic, M. Langer, and M. Douspis, Astron. Astrophys. **556,** A51 (2013).

[35] Y.-C. Cai, M. C. Neyrinck, I. Szapudi, S. Cole, and C. S. Frenk, Astrophys. J. **786,** 110 (2014).

[36] B. R. Granett, A. Kovács, and A. J. Hawken, Mon. Not. R. Astron. Soc. **454,** 2804 (2015).

[37] A. Kovács and B. R. Granett, Mon. Not. R. Astron. Soc. **452,** 1295 (2015).

[38] A. Kovács *et al.* (DES Collaboration), Mon. Not. R. Astron. Soc. **465,** 4166 (2017).

[39] C. L. Francis and J. A. Peacock, Mon. Not. R. Astron. Soc. **406,** 2 (2010).

[40] R. Scranton, A. J. Connolly, R. C. Nichol, A. Stebbins, I. Szapudi, D. J. Eisenstein, N. Afshordi, T. Budavari, I. Csabai, J. A. Frieman, J. E. Gunn, D. Johnston, Y. Loh, R. H. Lupton, C. J. Miller, E. S. Sheldon, R. S. Sheth, A. S. Szalay, M. Tegmark, and Y. Xu, arXiv:astro-ph/0307335.

[41] U. Sawangwit, T. Shanks, R. D. Cannon, S. M. Croom, N. P. Ross, and D. A. Wake, Mon. Not. R. Astron. Soc. **402,** 2228 (2010).

[42] B. Audren, J. Lesgourgues, K. Benabed, and S. Prunet, J. Cosmol. Astropart. Phys. 02 (2013) 001.

[43] J. Lesgourgues, W. Valkenburg, and E. Gaztanaga, Phys. Rev. D **77,** 063505 (2008).

[44] A. J. Nishizawa, Prog. Theor. Exp. Phys. **2014,** 6B110 (2014).

[45] D. N. Limber, Astrophys. J. **117,** 134 (1953).

[46] D. Blas, J. Lesgourgues, and T. Tram, J. Cosmol. Astropart. Phys. 07 (2011) 034.

[47] N. Aghanim *et al.* (Planck), Astron. Astrophys. **594,** A11 (2016).

[48] P. A. R. Ade *et al.* (Planck), Astron. Astrophys. **594,** A14 (2016).

[49] F. Beutler, C. Blake, M. Colless, D. H. Jones, L. Staveley-Smith, L. Campbell, Q. Parker, W. Saunders, and F. Watson, Mon. Not. R. Astron. Soc. **416,** 3017 (2011).

[50] A. J. Ross, L. Samushia, C. Howlett, W. J. Percival, A. Burden, and M. Manera, Mon. Not. R. Astron. Soc. **449,** 835 (2015).

[51] L. Anderson *et al.* (BOSS), Mon. Not. R. Astron. Soc. **441,** 24 (2014).

[52] A. Cuoco, M. Bilicki, J.-Q. Xia, and E. Branchini, Astrophys. J. Suppl. Ser. **232,** 10 (2017).

[53] M. Bilicki, T. H. Jarrett, J. A. Peacock, M. E. Cluver, and L. Steward, Astrophys. J. Suppl. Ser. **210,** 9 (2014).

[54] J. A. Peacock, N. C. Hambly, M. Bilicki, H. T. MacGillivray, L. Miller, M. A. Read, and S. B. Tritton, Mon. Not. R. Astron. Soc. **462,** 2085 (2016).

[55] T. H. Jarrett, T. Chester, R. Cutri, S. Schneider, M. Skrutskie, and J. P. Huchra, Astron. J. **119,** 2498 (2000).

[56] E. L. Wright, P. R. M. Eisenhardt, A. K. Mainzer *et al.*, Astron. J. **140,** 1868 (2010).

[57] D. Alonso, A. I. Salvador, F. J. Sánchez, M. Bilicki, J. García-Bellido, and E. Sánchez, Mon. Not. R. Astron. Soc. **449**, 670 (2015).

[58] L. Steward, Master's thesis, University of Cape Town, 2014.

[59] M. Bilicki, J. A. Peacock, T. H. Jarrett, M. E. Cluver, N. Maddox, M. J. I. Brown, E. N. Taylor, N. C. Hambly, A. Solarz, B. W. Holwerda, I. Baldry, J. Loveday, A. Moffett, A. M. Hopkins, S. P. Driver, M. Alpaslan, and J. Bland-Hawthorn, Astrophys. J. Suppl. Ser. **225**, 5 (2016).

[60] T. Goto, I. Szapudi, and B. R. Granett, Mon. Not. R. Astron. Soc. **422**, L77 (2012).

[61] A. Kovács, I. Szapudi, B. R. Granett, and Z. Frei, Mon. Not. R. Astron. Soc. **431**, L28 (2013).

[62] R. Beck, L. Dobos, T. Budavári, A. S. Szalay, and I. Csabai, Mon. Not. R. Astron. Soc. **460**, 1371 (2016).

[63] G. T. Richards, A. D. Myers, A. G. Gray, R. N. Riegel, R. C. Nichol, R. J. Brunner, A. S. Szalay, D. P. Schneider, and S. F. Anderson, Astrophys. J. Suppl. Ser. **180**, 67 (2009).

[64] J. J. Condon, W. D. Cotton, E. W. Greisen, Q. F. Yin, R. A. Perley, G. B. Taylor, and J. J. Broderick, Astron. J. **115**, 1693 (1998).

[65] G. de Zotti, M. Massardi, M. Negrello, and J. Wall, Astron. Astrophys. Rev. **18**, 1 (2010).

[66] I. Szapudi, S. Prunet, and S. Colombi, Astrophys. J. **561**, L11 (2001).

[67] G. Chon, A. Challinor, S. Prunet, E. Hivon, and I. Szapudi, Mon. Not. R. Astron. Soc. **350**, 914 (2004).

[68] G. Efstathiou, Mon. Not. R. Astron. Soc. **348**, 885 (2004).

[69] A. Challinor and G. Chon, Mon. Not. R. Astron. Soc. **360**, 509 (2005).

[70] J.-Q. Xia, A. Cuoco, E. Branchini, and M. Viel, Astrophys. J. Suppl. Ser. **217**, 15 (2015).

[71] S. D. Landy and A. S. Szalay, Astrophys. J. **412**, 64 (1993).

[72] G. Efstathiou, Mon. Not. R. Astron. Soc. **349**, 603 (2004).

[73] R. Takahashi, M. Sato, T. Nishimichi, A. Taruya, and M. Oguri, Astrophys. J. **761**, 152 (2012).

[74] M. Fornasa *et al.*, Phys. Rev. D **94**, 123005 (2016).

[75] F. Feroz, M. P. Hobson, and M. Bridges, Mon. Not. R. Astron. Soc. **398**, 1601 (2009).

[76] R. Trotta, arXiv:1701.01467.

[77] R. A. Sunyaev and Y. B. Zeldovich, Comments Astrophys. Space Phys. **4**, 173 (1972).

[78] M. J. Rees and D. W. Sciama, Nature (London) **217**, 511 (1968).

[79] P.-S. Corasaniti, T. Giannantonio, and A. Melchiorri, Phys. Rev. D **71**, 123521 (2005).

[80] L. Pogosian, P. S. Corasaniti, C. Stephan-Otto, R. Crittenden, and R. Nichol, Phys. Rev. D **72**, 103519 (2005).

[81] L. Pogosian, J. Cosmol. Astropart. Phys. 04 (2005) 015.

[82] E. V. Linder, Phys. Rev. Lett. **90**, 091301 (2003).

[83] M. Chevallier and D. Polarski, Int. J. Mod. Phys. D **10**, 213 (2001).

[84] W. Hu and I. Sawicki, Phys. Rev. D **76**, 104043 (2007).

[85] W. Fang, W. Hu, and A. Lewis, Phys. Rev. D **78**, 087303 (2008).

[86] S. Ando, A. Benoit-Lévy, and E. Komatsu, Mon. Not. R. Astron. Soc. **473**, 4318 (2018).

[87] L. Amendola *et al.*, arXiv:1606.00180.

[88] P. A. Abell *et al.* (LSST Science Collaboration), arXiv:0912.0201.

[89] M. Jarvis, D. Bacon, C. Blake, M. Brown, S. Lindsay, A. Raccanelli, M. Santos, and D. J. Schwarz, Advancing Astrophysics with the Square Kilometre Array (AASKA14) 18 (2015), arXiv:1501.03825.

[90] J. Renk, M. Zumalacárregui, F. Montanari, and A. Barreira, J. Cosmol. Astropart. Phys. 10 (2017) 020.

[91] K. M. Górski, E. Hivon, A. J. Banday, B. D. Wandelt, F. K. Hansen, M. Reinecke, and M. Bartelmann, Astrophys. J. **622**, 759 (2005).